



|                  |   |
|------------------|---|
| Title            | Circumpolar Mapping of Antarctic Coastal Polynyas and Landfast Sea Ice: Relationship and Variability  |
| Author(s)        | Nihashi, Sohey; Ohshima, Kay I.   |
| Citation         | Journal of climate, 28(9), 3650-3670<br><a href="https://doi.org/10.1175/JCLI-D-14-00369.1">https://doi.org/10.1175/JCLI-D-14-00369.1</a>   |
| Issue Date       | 2015-05-29  |
| Doc URL          | <a href="http://hdl.handle.net/2115/59557">http://hdl.handle.net/2115/59557</a>   |
| Rights           | © Copyright [29 January 2015] American Meteorological Society (AMS). Permission to use figures, tables, and brief excerpts from this work in scientific and educational works is hereby granted provided that the source is acknowledged. Any use of material in this work that is determined to be "fair use" under Section 107 of the U.S. Copyright Act September 2010 Page 2 or that satisfies the conditions specified in Section 108 of the U.S. Copyright Act (17 USC § 108, as revised by P.L. 94-553) does not require the AMS' s permission. Republication, systematic reproduction, posting in electronic form, such as on a web site or in a searchable database, or other uses of this material, except as exempted by the above statement, requires written permission or a license from the AMS. Additional details are provided in the AMS Copyright Policy, available on the AMS Web site located at ( <a href="http://www.ametsoc.org/">http://www.ametsoc.org/</a> ) or from the AMS at 617-227-2425 or <a href="mailto:copyrights@ametsoc.org">copyrights@ametsoc.org</a> . |
| Type             | article   |
| File Information | jcli-d-14-00369.1(1).pdf  |



[Instructions for use](#)

# Circumpolar Mapping of Antarctic Coastal Polynyas and Landfast Sea Ice: Relationship and Variability

SOHEY NIHASHI

*Department of Mechanical Engineering, National Institute of Technology, Tomakomai College, Tomakomai, Hokkaido, Japan*

KAY I. OHSHIMA

*Institute of Low Temperature Science, Hokkaido University, Sapporo, Hokkaido, Japan*

(Manuscript received 26 May 2014, in final form 29 January 2015)

## ABSTRACT

Sinking of dense water from Antarctic coastal polynyas produces Antarctic Bottom Water (AABW), which is the densest water in the global overturning circulation and is a key player in climate change as a significant sink for heat and carbon dioxide. Very recent studies have suggested that landfast sea ice (fast ice) plays an important role in the formation and variability of the polynyas and possibly AABW. However, they have been limited to regional and case investigations only. This study provides the first coincident circumpolar mapping of Antarctic coastal polynyas and fast ice. The map reveals that most of the polynyas are formed on the western side of fast ice, indicating an important role of fast ice in the polynya formation. Winds diverging from a boundary comprising both coastline and fast ice are the primary determinant of polynya formation. The blocking effect of fast ice on westward sea ice advection by the coastal current would be another key factor. These effects on the variability in sea ice production for 13 major polynyas are evaluated quantitatively. Furthermore, it is demonstrated that a drastic change in fast ice extent, which is particularly vulnerable to climate change, causes dramatic changes in the polynyas and possibly AABW formation that can potentially contribute to further climate change. These results suggest that fast ice and precise polynya processes should be addressed by next-generation models to produce more accurate climate projections. This study provides the boundary and validation data of fast ice and sea ice production for such models.

## 1. Introduction

Polynyas are defined as “any non-linear shaped opening enclosed within sea ice, and may contain brash ice and/or may be covered with new ice, nilas, or young ice” (WMO 1970). Polynyas have been classified into two types: “latent heat” polynyas and “sensible heat” polynyas. Most Antarctic coastal polynyas are latent heat polynyas, which are formed by divergent ice motion driven by winds and ocean currents (Morales Maqueda et al. 2004). Antarctic coastal polynyas are very high sea ice production areas (Markus et al. 1998; Renfrew et al. 2002; Tamura et al. 2008) because thin sea ice is a poor thermal barrier, permitting one or two orders of magnitude larger heat loss to the atmosphere than thick ice cover (Maykut 1978). In

the Antarctic Ocean, about 10% of sea ice is produced in the major coastal polynyas, although the total area of the polynyas is only about 1% of the maximum sea ice area (Tamura et al. 2008). The resultant large amount of brine rejection leads to the formation of dense water (Williams et al. 2008), which is a major source of Antarctic Bottom Water (AABW; Gordon et al. 1993; Comiso and Gordon 1998; Rintoul 1998; Williams et al. 2010; Ohshima et al. 2013). The sinking of the dense water plays a significant role in the global climate system by driving thermohaline (overturning) circulation (Killworth 1983) and biogeochemical cycles such as the carbon dioxide exchange between the atmosphere and deep ocean (Morales Maqueda et al. 2004; Miller and DiTullio 2007; Hoppema and Anderson 2007). The polynyas can also be biological “hot spots” during the spring and summer seasons because of much-enhanced primary productivity (Arrigo and van Dijken 2003).

Landfast sea ice (fast ice) is stationary sea ice attached to coastal features such as the shoreline and grounded

---

*Corresponding author address:* Sohey Nihashi, Department of Mechanical Engineering, National Institute of Technology, Tomakomai College, 443 Nishikioka, Tomakomai 059-1275, Japan.  
E-mail: sohey@me.tomakomai-ct.ac.jp

TABLE 1. Summary of statistics for the 13 major coastal polynyas. Here,  $S_a$  is average polynya area with daily standard deviation, CV is the coefficient of variation of the polynya area (ratio of the standard deviation of daily polynya area to the average polynya area), and  $V_a$  is the mean annual sea ice production with annual standard deviation. Daily data during wintertime (May–August) for the period 2003–11 are used for  $S_a$  and CV, and those during the freezing period (March–October) for the period 2003–10 are used for  $V_a$ . [Analysis areas are designated by yellow lines in Fig. 8; the areas are defined following the previous study (Tamura et al. 2008)].

| Polynya name           | Polynya area ( $S_a$ ; $10^3 \text{ km}^2$ ) | CV   | Ice production ( $V_a$ ; $10^{10} \text{ m}^3$ ) |
|------------------------|--|------|--|
| Cape Darnley (CDP)     | $10.3 \pm 3.7$                               | 0.36 | $13.4 \pm 1.3$                                   |
| Mackenzie Bay (MBP)    | $3.9 \pm 2.1$                                | 0.53 | $6.0 \pm 0.6$                                    |
| Barrier (BaP)          | $6.0 \pm 2.7$                                | 0.45 | $6.2 \pm 0.7$                                    |
| Shackleton (SP)        | $7.5 \pm 3.6$                                | 0.48 | $8.4 \pm 0.8$                                    |
| Vincennes Bay (VBP)    | $6.3 \pm 2.2$                                | 0.35 | $6.4 \pm 0.5$                                    |
| Dalton (DaP)           | $3.7 \pm 2.0$                                | 0.54 | $3.5 \pm 0.4$                                    |
| Dibble (DiP)           | $5.5 \pm 2.3$                                | 0.43 | $5.7 \pm 0.9$                                    |
| Mertz (MP)             | $9.7 \pm 4.4$                                | 0.45 | $13.2 \pm 1.9$                                   |
| Terra Nova Bay (TNBP)  | $3.6 \pm 2.1$                                | 0.58 | $5.9 \pm 0.6$                                    |
| Ross Ice Shelf (RISP)  | $17.7 \pm 10.6$                              | 0.60 | $30.0 \pm 2.2$                                   |
| Amundsen (AP)          | $7.7 \pm 3.6$                                | 0.46 | $9.0 \pm 1.4$                                    |
| Bellingshausen (BeP)   | $4.9 \pm 2.8$                                | 0.57 | $5.5 \pm 1.2$                                    |
| Ronne Ice Shelf (RONP) | $2.3 \pm 2.7$                                | 1.15 | $3.8 \pm 1.6$                                    |

icebergs (WMO 1970; Massom et al. 2001; Fraser et al. 2012). Previous studies have suggested that fast ice and glacier tongues play an important role in the formation of some coastal polynyas by blocking ice advection to cause divergence (Bromwich and Kurtz 1984; Massom et al. 1998, 2001). Particularly in East Antarctica, it has been suggested that polynyas are frequently formed on the western side of fast ice and glacier tongues probably because they block westward sea ice advection (Massom et al. 1998; Tamura et al. 2008). Key examples are the Mertz polynya (MP; abbreviations for major polynyas are summarized in Table 1) and Cape Darnley polynya (CDP), both of which are major source areas of AABW (Williams et al. 2010; Ohshima et al. 2013). Other polynyas forming adjacent to fast ice and glacier tongues are also possible candidates for AABW formation, for example, the Vincennes Bay polynya (VBP; Kitade et al. 2014). The Terra Nova Bay polynya (TNBP) also contributes to AABW formation in the Ross Sea (Kurtz and Bromwich 1985). Fast ice and glacier tongues are vulnerable to mechanical breaking and melting, and changes in their extent could affect the amount of the sea ice and dense water production in adjacent polynya. For example, the calving of the Mertz Glacier Tongue in February 2010 led to a substantial decrease in the MP area and sea ice production (Tamura et al. 2012; Dragon et al. 2014), which likely resulted in a reduction in dense water export and AABW production (Kusahara et al. 2011; Aoki et al. 2013; Lacarra et al. 2014). Significant changes in biogeochemical conditions also occurred (Shadwick et al. 2013).

To date, analysis of the role of fast ice and glacier tongues in polynya dynamics and associated AABW formation has been largely limited to regional and case studies only. A motivation of this study is to examine the

relationship between coastal polynyas and fast ice along the entire Antarctic coast. In the East Antarctic sector, Massom et al. (1998) summarized the locations of coastal polynyas that had been examined separately in earlier studies. Stand-alone circumpolar mapping of coastal polynyas has been carried out using satellite Special Sensor Microwave Imager (SSM/I) data (Tamura et al. 2008; Kern 2009). The large-scale mapping of fast ice has been carried out only along the East Antarctic coast using aircraft-observed data (Kozlovsky et al. 1977, cited in Fedotov et al. 1998), synthetic aperture radar (SAR) images (Giles et al. 2008), and cloud-free visible and infrared satellite images (Fraser et al. 2012).

In May 2002, the Advanced Microwave Scanning Radiometer for EOS (AMSR-E) was launched onboard NASA's *Aqua* satellite. Until it failed in October 2011, the AMSR-E sensor acquired brightness temperatures (TBs) regardless of darkness or cloud cover, as did the SSM/I. The spatial (grid) resolution of AMSR-E is 4 times higher than that of SSM/I in the pixel density. This advantage of AMSR-E is critical for the monitoring of coastal polynyas and fast ice because of their fairly small areal extent (i.e., from 10 to 100 km at most) (Tamura et al. 2008; Fraser et al. 2012). In this study, we present the first combined circumpolar mapping of Antarctic coastal polynyas (including their sea ice production) and fast ice, using AMSR-E data. The coincident detection of coastal polynyas and fast ice using same satellite sensor is also an advantage for investigating their relationship.

## 2. AMSR-E algorithms

For the circumpolar mapping, thin ice thickness estimation and fast ice detection algorithms for AMSR-E

have been developed based on algorithms for SSM/I (Tamura et al. 2007). The daily mean ice thickness and monthly fast ice datasets were created from March to October for the period 2003–11 (March–September only for 2011). These AMSR-E datasets were mapped onto the National Snow and Ice Data Center (NSIDC) polar stereographic grid with about 6.25-km grid resolution. This grid has its tangential plane and hence minimum distortion at 70°S, around which most of Antarctic coastal polynyas are formed.

#### a. Estimation of thin ice thickness

On the basis of comparisons between TBs obtained from passive microwave radiometer onboard a ship and sea ice data from in situ measurements in the Canadian Arctic, Hwang et al. (2007) showed that a ratio of the vertically to horizontally polarized TBs ( $R = TB_V/TB_H$ ) is negatively correlated with thin ice thickness of less than about 0.2 m, where  $TB_V$  and  $TB_H$  are the vertically and horizontally polarized TBs, respectively. They also showed that salinity of the ice surface is strongly correlated with the thin ice thickness, indicating that the negatively correlated relationship between the  $R$  and ice thickness is primarily caused by the ice surface salinity. Similar relationships between ice salinity and thin ice thickness have been also shown by several other observations (Cox and Weeks 1983; Kovacs 1996; Toyota et al. 2007). These results suggest that thin ice thickness of less than about 0.2 m can be estimated from the  $R$ . In situ measurements have shown that ice thickness in Antarctic coastal polynyas is generally less than about 0.2 m (Jeffries and Adolphs 1997; Tamura et al. 2006). In this study, ice thickness of  $\leq 0.2$  m is estimated from polarization ratio (PR) of TBs, as in previous studies (Tamura et al. 2007; Nihashi et al. 2009; Iwamoto et al. 2013, 2014). PR is defined by  $PR = (TB_V - TB_H)/(TB_V + TB_H)$  and linearly transformed from  $R$  using the equation  $PR = (R - 1)/(R + 1)$ . We used the AMSR-E/Aqua Level 2A (L2A) global swath spatially resampled brightness temperatures (Ashcroft and Wentz 2003) at 89 and 36.5 GHz, with footprint sizes of  $6 \text{ km} \times 4 \text{ km}$  and  $14 \text{ km} \times 8 \text{ km}$ , respectively. Because of the higher spatial resolution, TBs at 89 GHz can minimize the effects of land, ice shelf, and fast ice contamination in the area close to the coast and fast ice, where thinner ice is dominant. On the other hand, the 89-GHz data possibly misclassify fast ice as thin ice, especially for the thickness range of  $>0.1$  m (Iwamoto et al. 2014; see also next subsection). In this study, ice thickness estimated from TBs at 89 GHz is used for thickness range of  $\leq 0.1$  m, and ice thickness estimated from TBs at 36.5 GHz, having a relatively deeper penetration depth, is used for thickness range of 0.1–0.2 m.

This method was also adopted in Tamura et al. (2007) and Iwamoto et al. (2014).

A thin ice thickness algorithm has been developed from comparisons between the PR and ice thickness based on heat flux calculations with ice surface temperatures from satellite thermal infrared images (Yu and Rothrock 1996). The ice thickness is estimated from conductive heat flux in ice by assuming that it balances with the heat flux between ice and atmosphere. The snow cover on ice was neglected because new ice generally does not have a significant amount of snow. We used channel 31 and 32 images from the NASA Moderate Resolution Imaging Spectroradiometer (MODIS) on Aqua, which is the same platform as that of AMSR-E. Specifically, MODIS Level 1B swath data provided by NASA's Level 1 and Atmosphere Archive and Distribution System website (LAADS web; <http://ladsweb.nascom.nasa.gov/>) were used. The footprint size is about 1.1 km. We chose MODIS images that are free from cloud cover and ice fog during polar night, when shortwave radiation is negligible. Thus, the heat flux between ice and atmosphere is the sum of net longwave radiation and turbulent heat flux. The ice surface temperatures were calculated using the empirical equation proposed by Key et al. (1997) with modification for the MODIS data (Hall et al. 2004; Riggs et al. 2006; Scambos et al. 2006). Ice bottom temperature was set to the freezing point of  $-1.86^\circ\text{C}$ .

Heat fluxes were calculated using formulas that are suitable for the Antarctic sea ice zone, following Nihashi and Ohshima (2001). Specifically, the longwave radiation is calculated by an empirical formula (König-Langlo and Augstein 1994). The turbulent heat fluxes are calculated from bulk formulas (Maykut and Perovich 1987). We use the bulk transfer coefficients proposed by Kondo (1975), which incorporate the stability effect of the atmospheric surface layer. As atmospheric input data, we used near-surface atmospheric data from the 6-hourly ECMWF interim reanalysis (ERA-Interim) dataset with a spatial resolution of  $0.5^\circ \times 0.5^\circ$ . Data of air temperature at 2 m, dewpoint temperature at 2 m, wind at 10 m, and surface sea level pressure (SLP) were used. The ERA-Interim data were interpolated onto the MODIS data points using a Gaussian weighting function.

For the comparison with AMSR-E data, the MODIS ice thickness with a spatial resolution of about 1 km was remapped onto the data points of AMSR-E L2A data. There are dozens of MODIS pixels within the footprint of AMSR-E. We used the thermal ice thickness for which the calculated total heat flux using MODIS data would be realized under the assumption of uniform ice thickness in the AMSR-E footprint (Drucker et al. 2003;

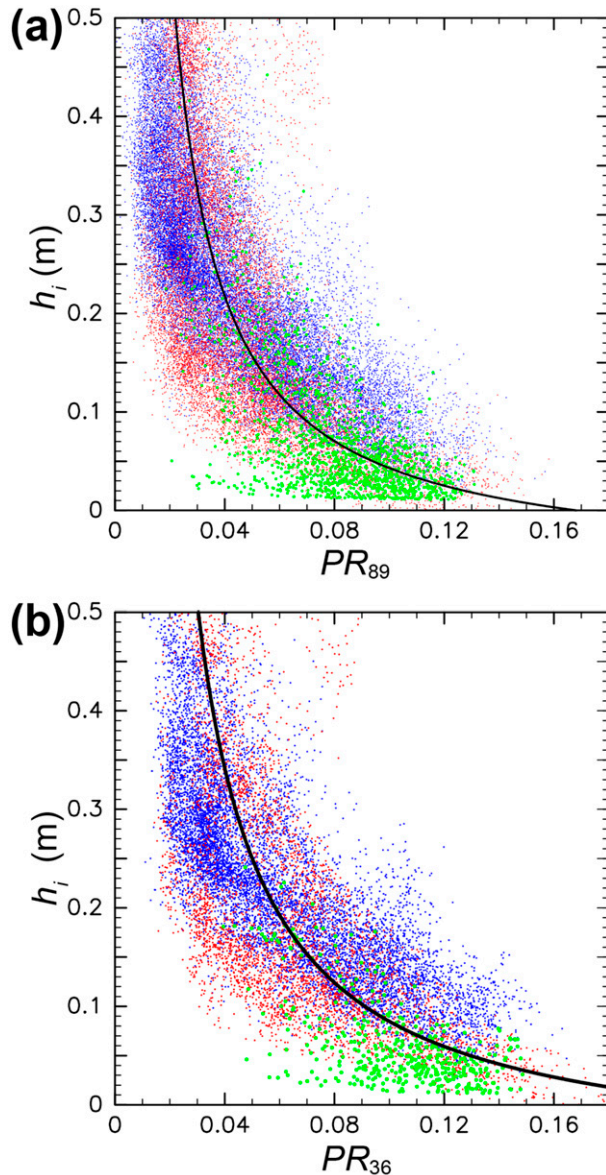


FIG. 1. (a) Scatterplot of  $PR_{89}$  vs  $h_i$ . (b) As in (a), but for use of  $PR_{36}$ . Blue, red, and green dots indicate data from areas of the Ross Ice Shelf polynya, Ronne Ice Shelf polynya, and Cape Darnley polynya, respectively. The exponential curve that best fits to the plots is superimposed.

Tamura et al. 2007). The thermal ice thickness does not exactly coincide to the arithmetic average of the thicknesses that are calculated at MODIS pixels within the AMSR-E footprint. This thermal ice thickness ( $h_i$ ) is suitable for heat loss calculation in estimation of ice production.

A scatterplot of the PR at 89 GHz ( $PR_{89}$ ) versus  $h_i$  is shown in Fig. 1a. We used 60 clear-sky MODIS images from areas of the Ross Ice Shelf polynya (RISP; 22 scenes), Ronne Ice Shelf polynya (RONP) in the

TABLE 2. Summary of statistics between  $h_i$  from MODIS vs  $h_{89}$  and  $h_{36}$  from AMSR-E for the Ross Ice Shelf polynya, Ronne Ice Shelf polynya, Cape Darnley polynya, and all of the three areas, with the number of samples. RMSD and SD are the root-mean-square deviation and the standard deviation, respectively. Bias is  $h_i$  minus  $h_{89}$  or  $h_{36}$ .

|   | RISP | RONP | CDP  | All  |
|---|------|------|------|------|
| $h_{89} \leq 10$ cm ( $PR_{89} \geq 0.067$ )              |      |      |      |      |
| RMSD (cm)   | 6.9  | 3.5  | 3.3  | 5.8  |
| SD (cm)   | 4.2  | 3.4  | 3.3  | 4.6  |
| Bias (cm)   | 5.5  | 0.9  | -0.6 | 3.5  |
| Sample No.  | 5014 | 2281 | 1095 | 8390 |
| $10 < h_{36} \leq 20$ cm ( $0.059 < PR_{36} \leq 0.091$ ) |      |      |      |      |
| RMSD (cm)   | 5.3  | 5.7  | 6.7  | 5.5  |
| SD (cm)   | 4.4  | 5.6  | 4.9  | 5.2  |
| Bias (cm)   | 2.9  | 0.2  | -4.6 | 1.7  |
| Sample No.  | 2129 | 1264 | 108  | 3501 |

Weddell Sea (27 scenes), and CDP (11 scenes); these were acquired during April–September from 2006 to 2008. These polynyas are major source areas of AABW (Jacobs et al. 1970; Foster and Carmack 1976; Ohshima et al. 2013). For the plot, we used the AMSR-E swath data that were taken at the closest time to when the MODIS image was acquired. The  $PR_{89}$  value is negatively correlated with  $h_i$ . The relationships for the three polynya areas are roughly similar. A scatterplot of the PR at 36.5 GHz ( $PR_{36}$ ) versus  $h_i$  (Fig. 1b) also shows a negatively correlated relationship. A similar negatively correlated relationship has been shown from data in the Arctic Ocean, Sea of Okhotsk, and along the Labrador coast, and also from SSM/I data (Martin et al. 2004; Tamura et al. 2007; Nihashi et al. 2009; Tamura and Ohshima 2011; Iwamoto et al. 2013, 2014; Scott et al. 2014).

In this study, an exponential curve which best fits into the scatterplot of the PR versus  $h_i$  was used, following previous studies (Martin et al. 2004; Iwamoto et al. 2013, 2014). For the fitting, the normal from each data to the curve was calculated for all data with  $h_i$  of  $< 0.3$  m, and then a least squares fitting was applied to minimize the distance. The derived equations using all data of the three polynya areas are

$$h_{89} = e^{1/102 PR_{89}} - 1.06, \quad \text{and} \quad (1)$$

$$h_{36} = e^{1/74 PR_{36}} - 1.06. \quad (2)$$

The curves given in Eqs. (1) and (2) are superimposed on Fig. 1.

Statistics of  $h_i$  versus  $h_{89}$  and  $h_{36}$  are summarized in Table 2. The root-mean-square deviations between the curve and  $h_i$  are 5.8 cm for the  $PR_{89}$  value of  $\geq 0.067$

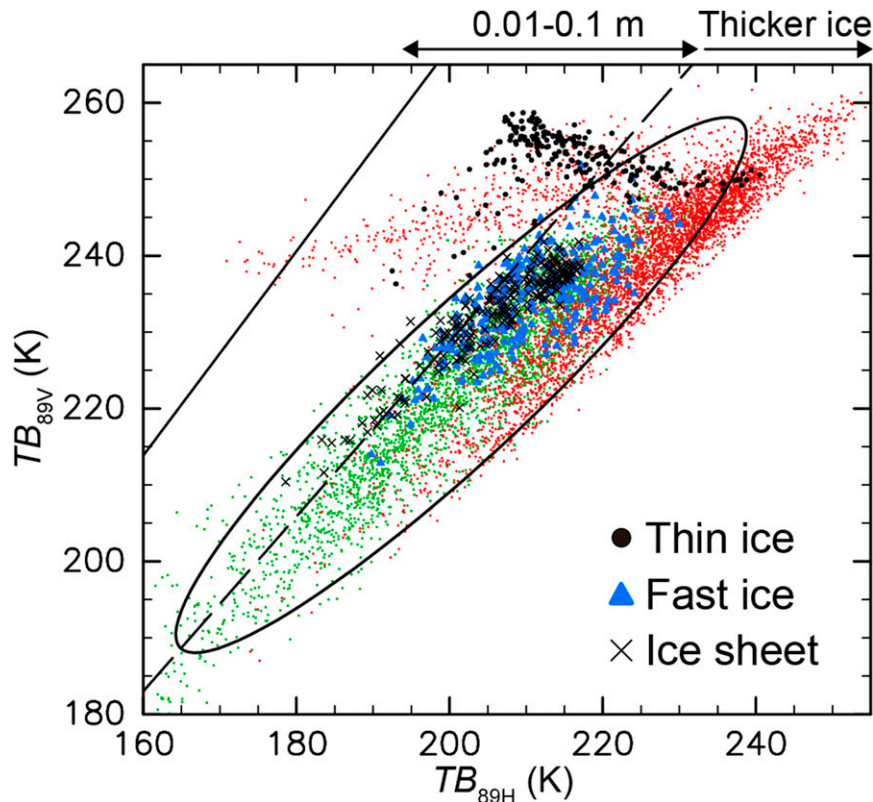


FIG. 2. Scatterplot of horizontally vs vertically polarized AMSR-E brightness temperatures (TBs) at 89 GHz on 28 Aug 2010. (Red and green dots indicate the data for the red and green areas in Fig. 3, respectively.) From a comparison with a visible image from MODIS in the Barrier polynya area (Fig. 12e; the area is designated by a rectangle in Fig. 3), TBs whose pixels are selected as thin ice, fast ice, and ice sheet are shown by black dots, blue triangles, and black crosses, respectively. A solid line indicates a  $PR_{89}$  value of 0.144 corresponding to ice thickness of 0.01 m. A dashed line indicates a  $PR_{89}$  value of 0.067 corresponding to ice thickness of 0.1 m. An ellipse derived from the principal component analysis using the TBs over the Antarctic continent (green dots) is superimposed.

(corresponding to an ice thickness of  $\leq 10$  cm) and 5.5 cm for the  $PR_{36}$  value of 0.059–0.091 (corresponding to an ice thickness of 10–20 cm). For data of the three polynya areas, the bias of  $h_i$  minus  $h_{89}$  for the  $PR_{89}$  value of  $\geq 0.067$  is from  $-0.6$  to  $5.5$  cm; the bias of  $h_i$  minus  $h_{36}$  for the  $PR_{36}$  value of 0.059–0.091 is from  $-4.6$  to  $2.9$  cm. The values of these deviations and biases are generally within the accuracy of  $h_i$  (about  $\pm 5$  cm) defined from the comparisons with in situ observations (Drucker et al. 2003; Tamura et al. 2006; Nihashi et al. 2009). Therefore, we used Eqs. (1) and (2) as the unified algorithm for the estimation of thin ice thickness over the entire Antarctic Ocean.

Ice thickness calculated using AMSR-E swath data at 89 and 36.5 GHz ( $h_{89}$  and  $h_{36}$ ) is mapped onto the NSIDC polar stereographic grid at a spatial resolution of about 6.25 km and about 12.5 km, respectively, and then daily mean thickness is calculated. Because a grid

cell of the 12.5-km NSIDC grid is set to correspond to four grid cells of the 6.25-km NSIDC grid,  $h_{89} \leq 0.1$  m and  $h_{36}$  of 0.1–0.2 m with the two spatial resolutions can be merged directly.

TBs at 89 GHz tend to be influenced by cloud cover, ice fog, and water vapor to a greater extent than TBs at 36.5 GHz. This leads to smaller values of  $PR_{89}$ , and thus  $h_{89}$  is overestimated (Tamura et al. 2007). In this study, because the atmospheric influence is less at 36.5 GHz,  $h_{89}$  is replaced with  $h_{36}$  of the corresponding pixel if  $h_{89} \geq h_{36}$ ; thereby about 20% of total  $h_{89}$  pixels were replaced. We also have confirmed that  $h_{89}$  and  $h_{36}$  coincide with each other with the root-mean-square deviation of about 1–2 cm in the case of a clear sky (not shown).

The algorithm of Eqs. (1) and (2) can be used to detect only thin ice and its thickness, and thus the first-year ice and open water area must be detected using

a different method. For that purpose, we used daily mean ice concentration based on the enhanced National Aeronautics and Space Administration (NASA) Team (NT2) algorithm (Markus and Cavalieri 2000). The ice concentration is mapped on the polar stereographic grid at a spatial resolution of about 12.5 km. In this study, open water is defined as the area where the ice concentration is  $<30\%$ , following Nihashi et al. (2009) and Iwamoto et al. (2014). Among the remaining pixels, those whose thickness is estimated to be  $>0.2$  m in the thin ice algorithm are labeled as first-year ice.

### b. Detection of fast ice

In the Antarctic Ocean, fast ice is formed along the coast, and the fast ice extent is changed by mechanical breaking, melting, and regeneration. Antarctic coastal polynyas tend to be formed adjacent to fast ice. The AMSR-E thin ice thickness algorithm possibly misclassifies fast ice as thin ice because the  $PR_{89}$  values of thin ice and fast ice can be similar for a certain thickness range (Kern et al. 2007; Tamura et al. 2007), especially for  $h_{89} > 0.1$  m (Iwamoto et al. 2014). Thus, the independent detection of fast ice is essential for accurate polynya detection.

A fast ice detection algorithm has been developed based on a relationship between horizontally and vertically polarized AMSR-E TBs at 89 GHz (Fig. 2), where daily mean TBs (Cavalieri et al. 2004) were used. Red and green dots in Fig. 2 indicate TBs over the area for fast ice detection (red area in Fig. 3) and over the Antarctic continent close to the coast (green area in Fig. 3), respectively. For the comparison, TBs of thin ice, fast ice, and ice sheet in the Barrier polynya (BaP) area are superimposed on Fig. 2. These three ice types were visually selected by using a MODIS image. In this scatterplot, TBs within a domain between solid and dashed lines are regarded as thin ice of 0.01–0.1 m by the thin ice thickness algorithm. However, some fast ice TBs exist in this domain, implying that fast ice is possibly misclassified as thin ice by the ice thickness algorithm. On the other hand, the plot also shows that the TBs of fast ice tend to be lower than those of thin ice and are similar to those of ice sheet [see also Fig. 9 in Tamura et al. (2007)], probably because the fast ice, which is usually covered with thick snow with no leads, has a surface condition closer to that of the ice sheet than that of thin ice.

Based on these microwave characteristics, fast ice is detected. On the daily scatterplot (Fig. 2), an ellipse is defined based on a principal component analysis using the TBs over the Antarctic continent (green dots). The ellipse is drawn from the center of gravity of the cluster

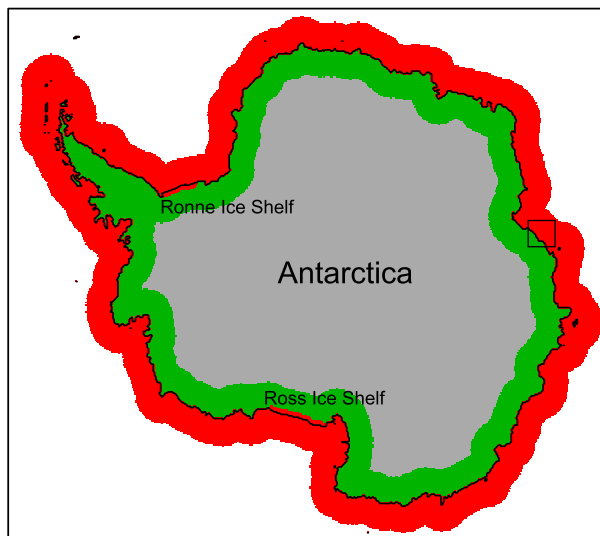


FIG. 3. Analysis areas for the AMSR-E fast ice detection. The areas are made based on a fixed land mask of Antarctica at a spatial resolution of about 12.5 km provided by NSIDC (the coastline shown by black lines indicates the land mask). Fast ice detection is made in the red area defined as areas where the distance from the coastline to the offshore is  $\leq 250$  km and areas where the distance from the coastline to the inland is  $\leq 12.5$  km ( $\leq 50$  km at the Ronne and Ross Ice Shelves). An ellipse for the fast ice detection (Fig. 2) is constructed by using brightness temperatures in the green area defined as ones where the distance from the coastline is  $\leq 250$  km, except for within the red area defined above. A box indicates the Barrier polynya area that is used for a comparison between AMSR-E TBs and a MODIS visible image in Fig. 2.

of points, where the first and second principal component axes are set to the major and minor axes, respectively, with the amplitude being 2.5 times the standard deviation for each component (Fig. 2). From the comparison with a clear-sky MODIS image, about 99% of the ice sheet pixels exist inside this ellipse. About 1% of the fast ice pixels do not lie inside the ellipse, while about 22% of the thin ice pixels are inside the ellipse. It is difficult to discriminate fast ice from first-year and thin ice on a daily basis. Fast ice is much more stable when compared to the daily drifting first-year and thin ice. Thus, the use of longer period data is effective for the fast ice detection. For making the monthly fast ice dataset, we use TBs for three consecutive months including the previous and following months. The specific process is as follows. First, the daily ellipse was calculated for the three months. Then the pixels that were classified as fast ice with the frequency exceeding 70% of the 3-month period were detected as fast ice pixels of the central month. Although the data used overlap with the previous and next months, this method resolves the monthly variation to some extent. If fast ice was detected using TBs only for a month, some false fast ice pixels appear

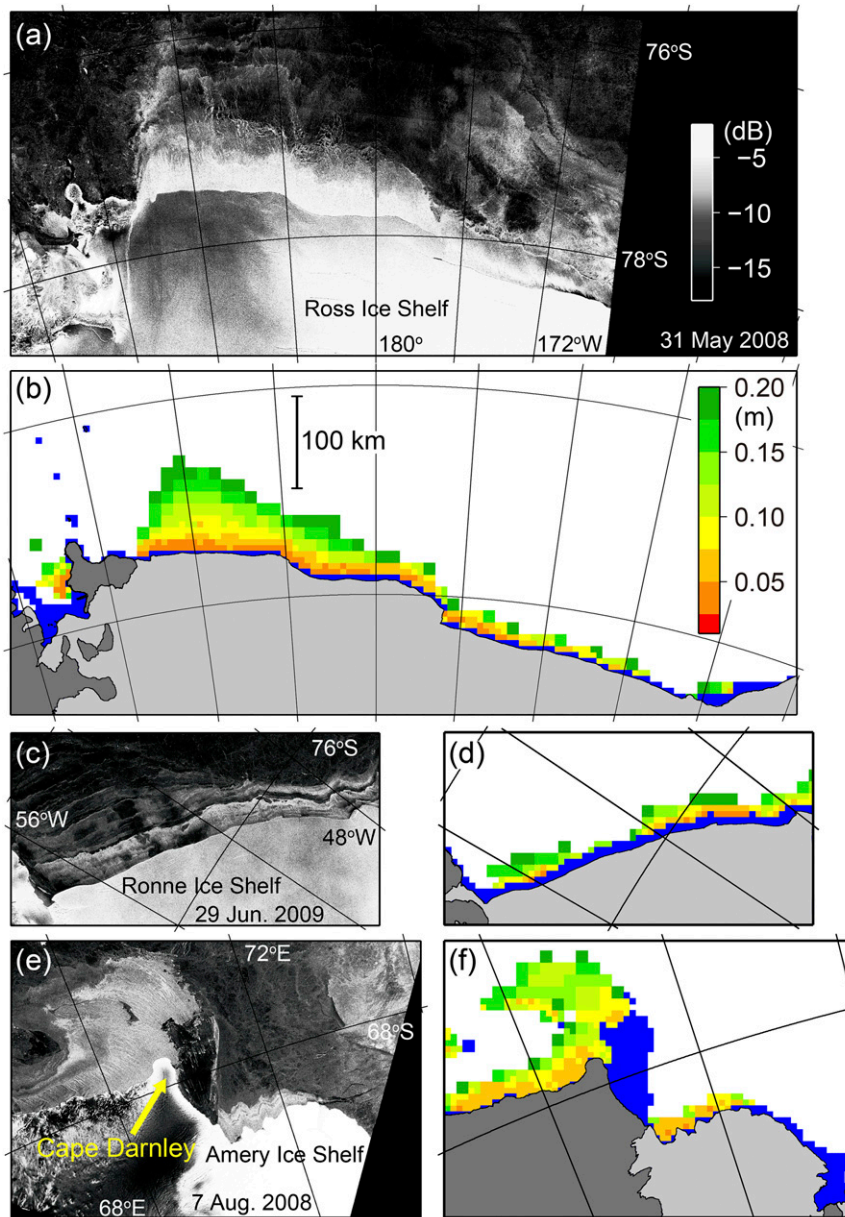


FIG. 4. Sea ice backscatter and thin ice thickness in (a),(b) the Ross Ice Shelf polynya area on 31 May 2008, (c),(d) the Ronne Ice Shelf polynya area on 29 Jun 2009, and (e),(f) the Cape Darnley polynya and Mackenzie Bay polynya areas on 7 Aug 2008. For (a),(c), and (e), radar backscatter images from *Envisat* ASAR are shown. The backscatter was obtained by taking into account the calibration and the incidence angle. For (b),(d), and (f), thin ice thickness and fast ice (blue) from AMSR-E are shown. Fast ice of the corresponding month is shown. The spatial scale is the same for all the panels.

patchily in first-year and thin ice areas (not shown). Also in the fast ice detection by SSM/I (Tamura et al. 2007), monthly fast ice was detected using daily data for the three consecutive months. The monthly fast ice data were created from March to October for the period of 2003–10 using daily TBs for three months during February–November. In 2011, the monthly data were

created from March to September; the dataset in September 2011 was created using TBs for two months of August–September because the AMSR-E failed in October 2011. This fast ice dataset also includes the variable ice shelf edge, glacier tongues, and grounded iceberg tongues because the microwave characteristic of these is similar to that of ice sheet.

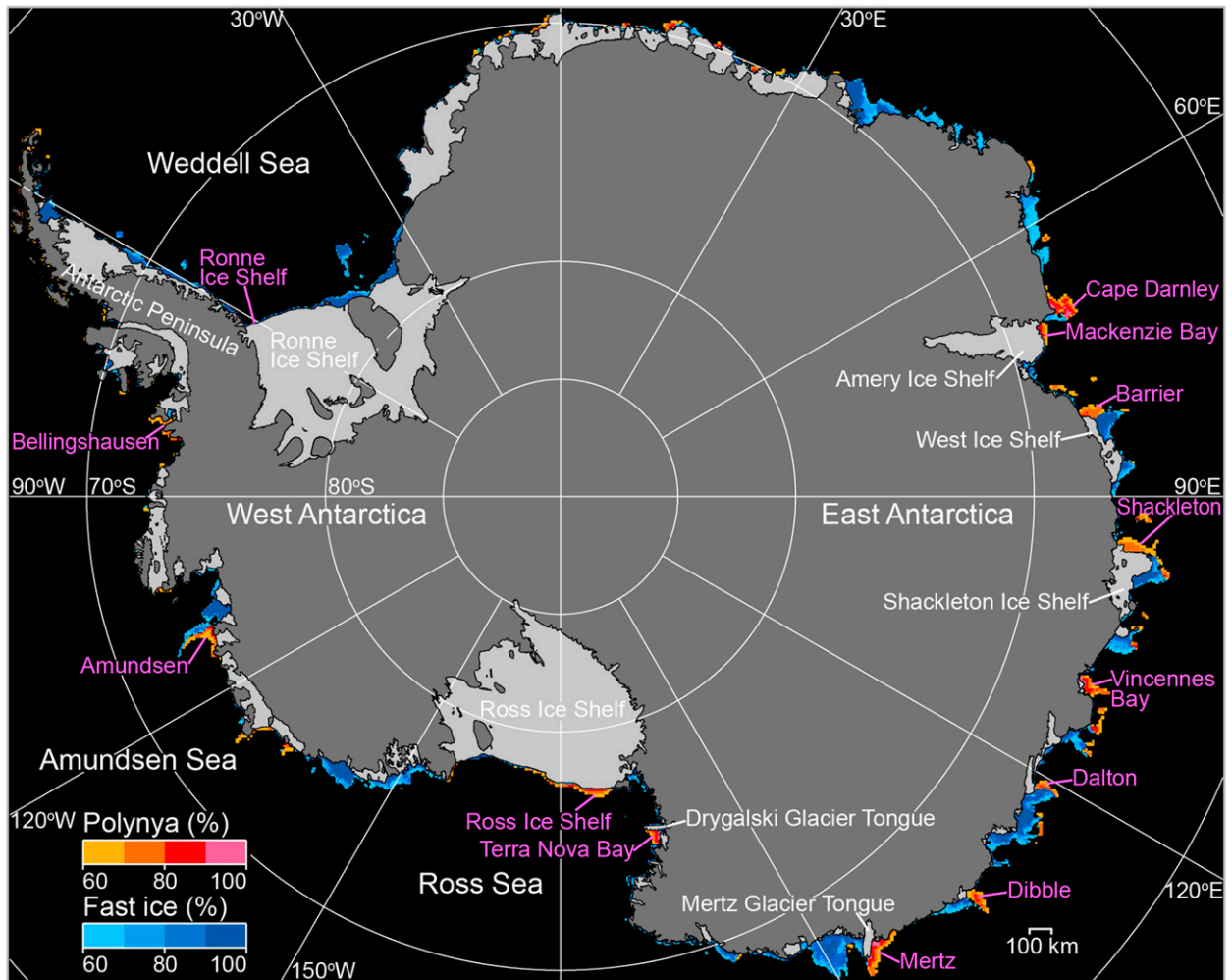


FIG. 5. Map of Antarctic coastal polynyas and landfast sea ice from AMSR-E. Frequency of occurrence during the freezing period (March–October) for the period 2003–11 (March–September only for 2011) is shown by color shadings. Fast ice pixels in the Weddell Sea detached from the coastline is the grounded iceberg A23-A. The Antarctic continent and islands are indicated by gray, and ice shelves and glacier tongues are indicated by light gray.

### c. Comparison with SAR images

For the RISP, RONP, CDP, and Mackenzie Bay polynya (MBP) areas, thin ice and fast ice estimates from AMSR-E were compared with >100 SAR images (including quick look images) acquired by the Advanced Synthetic Aperture Radar (ASAR: C-band SAR; the wavelength is 5.6 cm) on the European Space Agency's (ESA) *Environmental Satellite (Envisat)*. The spatial resolution of the ASAR image (about 150 m) is much higher than that of AMSR-E. In most cases, the thin ice and fast ice areas detected from the AMSR-E data corresponded well with those presumed from the ASAR image. Here we show some examples. Figures 4a, 4c, and 4e show radar backscatter images from ASAR. White streaks with high backscatter ( $> -10$  dB) are shown in

each polynya area, and this area is considered to be covered with newly formed sea ice. The thin ice ( $\leq 0.2$  m) area detected by AMSR-E (Figs. 4b,d,f) corresponds to the new ice area seen in the ASAR image to some extent. A low backscatter ( $< -15$  dB) area with small patches of high backscatter ( $> -5$  dB) exists east of the CDP (Fig. 4e). It can be considered that the low backscatter area is the fast ice anchored by small grounded icebergs indicated by the high backscatter patches (Fraser et al. 2012). The fast ice area detected by AMSR-E corresponds well with the area of fast ice with grounded icebergs seen in the ASAR image (Figs. 4e,f). Comparisons with clear-sky visible images by MODIS also support the reliability of the AMSR-E algorithms; the examples in the MP and BaP areas are shown later in section 3d (Figs. 10 and 12).

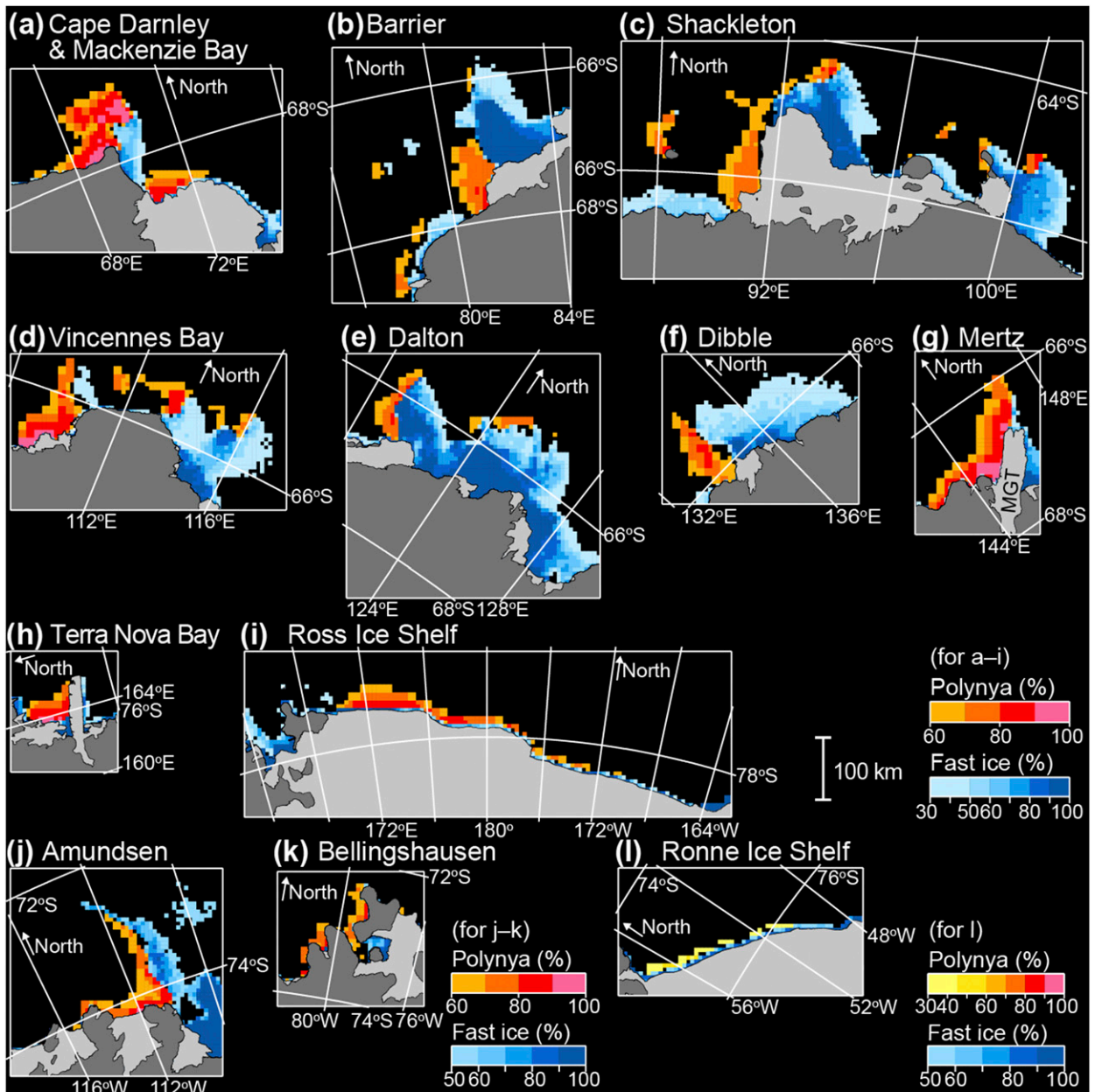


FIG. 6. Close-up maps of coastal polynyas and landfast sea ice from AMSR-E for (a)–(l) the 13 major polynya areas of high sea ice production (Tamura et al. 2008). Frequency of occurrence during the freezing period for the period 2003–11 is shown by color shadings. Note that the color shadings for (j)–(l) are different from the others. The Antarctic continent and islands are indicated by gray, and ice shelves and glacier tongues are indicated by light gray. The spatial scale is the same for all the panels.

### 3. Results and discussion

At the beginning of the freezing season (March–April), the advancing thin ice area might not be regarded as a coastal polynya (thin ice area enclosed by pack ice). Even in that case, ice production in the thin ice area contributes to dense water formation. In this study, maps of coastal polynyas (sea ice production) and fast ice are

created using data during the entire freezing period of March–October, also following Tamura et al. (2008). On the other hand, for an analysis in which the polynya area is used, we use the data only during wintertime (after May). To analyze the data for entire 9-yr period of AMSR-E, the data until August are used because the AMSR-E ice thickness is available only until the middle of September 2011.

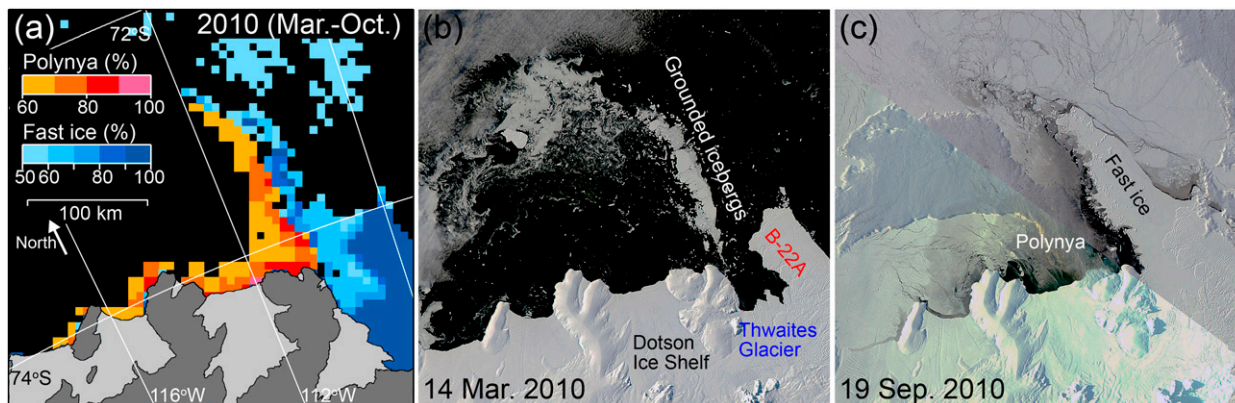


FIG. 7. Close-up maps of sea ice condition in the Amundsen polynya area. (a) Frequency of occurrence of coastal polynyas and fast ice from AMSR-E during the freezing period in 2010. (b),(c) Visible images from MODIS.

### a. Mapping of coastal polynyas and fast ice

The frequency of occurrence of coastal polynyas and fast ice using AMSR-E data are shown in Fig. 5. The map reveals the circumpolar distributions of fast ice in the Antarctic Ocean for the first time. Close-up maps of each coastal polynya and fast ice are presented in Fig. 6, revealing their detailed spatial distributions. The coastline, ice shelf, and glacier tongue locations were obtained from the NSIDC high-resolution Mosaic of Antarctica 2003–2004 (MOA2004) dataset with a spatial resolution of about 125 m (Haran et al. 2005).

A similar map of fast ice covering the period March 2000–December 2009 has been shown by Fraser et al. (2012) but only for the East Antarctic sector. The fast ice map in this study is similar to that (Fig. 2) in Fraser et al. (2012), except that the frequency of this study is relatively lower, especially for the coastal areas around 30° and 165°E. This difference might be because newly formed fast ice whose TBs are similar to those of thin or first-year ice is more difficult to detect by the method of this study.

In the West Antarctic sector, fast ice is mainly located along the Amundsen Sea, the eastern side of the Antarctic Peninsula, and east of the Ronne Ice Shelf. A remarkable feature in the West Antarctic sector is fast ice that extends far (>100 km) in the meridional direction but is zonally limited in the Amundsen Sea (Figs. 6j and 7a). Visible images from MODIS (Figs. 7b,c) suggest that the fast ice is formed by the anchor points of grounded icebergs as in the CDP (Figs. 4e,f). This was also pointed out by Nakayama et al. (2014).

The coincident maps of coastal polynyas and fast ice (Figs. 5 and 6) clearly reveal their close relationship:

many larger polynyas (Table 1), such as the CDP, BaP, Shackleton polynya (SP), VBP, Dalton polynya (DaP), Dibble polynya (DiP), and Amundsen polynya (AP) are formed on the western side of fast ice, while the MP and TNBP are formed adjacent to glacier tongues with fast ice (Figs. 6g,h). These findings suggest that fast ice (and glacier tongues) is an essential element for the formation of most of the Antarctic coastal polynyas.

### b. Relationships between the polynya area and wind

Wind is thought to be the main forcing for coastal polynya formation (Zwally et al. 1985; Pease 1987; Adolphs and Wendler 1995; Markus and Burns 1995; Massom et al. 1998; Comiso et al. 2011; Drucker et al. 2011). In the present paper, the relationship between the polynya area and the wind is evaluated for the 13 major polynyas of high sea ice production on the basis of correlation analysis. In general, ice motion approximately follows the geostrophic wind (Thorndike and Colony 1982). We used the geostrophic winds calculated based on the SLP from the daily mean ERA-Interim. Maps of average geostrophic wind confirm that the easterly winds prevail around the Antarctic coastal margin, except in the Ross and Weddell Sea sectors (Fig. 8). To find the wind component that is most effective for polynya formation and that determines polynya area variability, we calculate correlation coefficients between the daily polynya area  $S_d$  and components of the wind vector projected in all directions of every 1° from 0° (northerly wind) clockwise to 360°. The correlation coefficient  $r$  and direction  $\theta$  for the wind component with the highest correlation are shown in Table 3 and Fig. 8. This wind component is defined as  $U_{\text{rmax}}$ . The value of

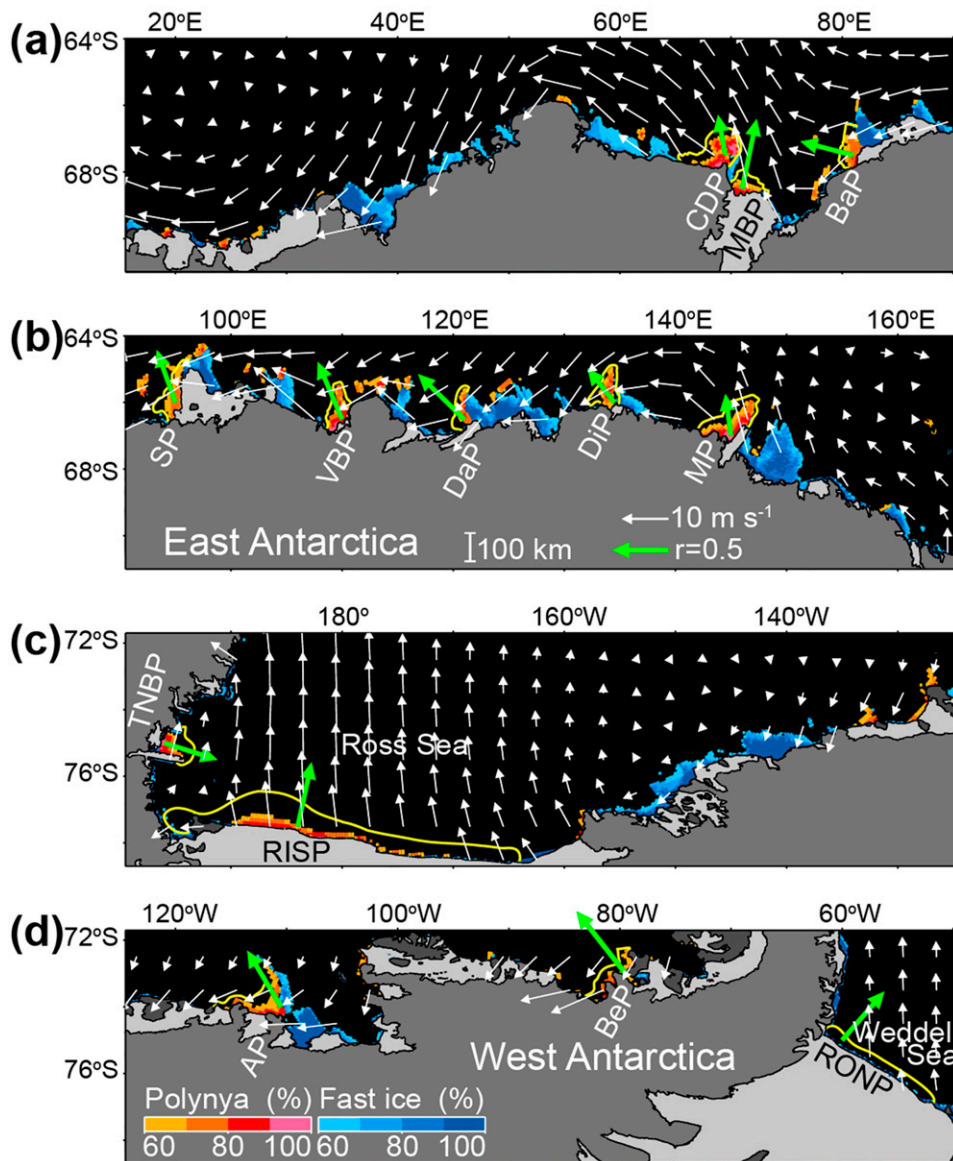


FIG. 8. Geostrophic wind vectors (white arrows) averaged during wintertime (May–August) over 2003–11. Green arrows indicate the correlation coefficient  $r$  (shown by the length) and the direction  $\theta$  of the geostrophic wind component which best correlates with the polynya area. The scale of the wind vector and correlation coefficient are shown at the bottom of Fig. 8b. The values of  $r$  and  $\theta$  are summarized in Table 3. Frequency of occurrence of coastal polynya and fast ice (Fig. 5) is superimposed. The polynya abbreviations follow Table 1.

$r$  increases when the wind is temporally averaged using data for the previous three days or more (not shown). The polynya edge would advance about 40 km over the 3-day period, when a geostrophic wind of  $10 \text{ m s}^{-1}$  continues in the direction of advance (Fig. 8) and the wind-forced ice drift is assumed to be 1.5% of the geostrophic wind speed (Kottmeier and Sellmann 1996; Vihma et al. 1996; Uotila et al. 2000). This spatial scale corresponds to the typical windward extent

of the Antarctic coastal polynyas (Fig. 8), indicating that three days is an appropriate time scale of the wind that determines the polynya area. In this study, the wind averaged for the previous three days is used. In Table 3, the results using the SLP from the National Centers for Environmental Prediction Climate Forecast System Reanalysis (NCEP CFSR) with a spatial resolution of  $0.5^\circ \times 0.5^\circ$  (Saha et al. 2010) are also presented.

TABLE 3. Summary of a correlation coefficient ( $r$ ) and direction ( $\theta$ ) of a wind component ( $U_{\text{max}}$ ) which shows the highest correlation with the polynya area ( $S_d$ ) for the major coastal polynyas. Geostrophic winds calculated based on the SLP near the grid points for each polynya were used. Note that  $S_d$  is calculated in the area designated by yellow lines in Fig. 8; the areas are defined following the previous study (Tamura et al. 2008). The daily data during wintertime (May–August) from 2003 to 2011 (from 2003 to 2010 for NCEP CFSR) were used. All of the  $r$  values are significant at 99.5%. The  $\theta$  values of  $0^\circ$  and  $90^\circ$  correspond to northerly and easterly wind components, respectively. The results in the ERA-Interim columns are also shown in Fig. 8 by green arrows.

| Polynya | ERA-Interim |                       | NCEP CFSR |                       |
|---------|-------------|-----------------------|-----------|-----------------------|
|         | $r$         | $\theta$ ( $^\circ$ ) | $r$       | $\theta$ ( $^\circ$ ) |
| CDP     | 0.37        | 151                   | 0.36      | 137                   |
| MBP     | 0.64        | 212                   | 0.56      | 222                   |
| BaP     | 0.49        | 95                    | 0.59      | 98                    |
| SP      | 0.50        | 133                   | 0.47      | 128                   |
| VBP     | 0.56        | 128                   | 0.51      | 138                   |
| DaP     | 0.58        | 108                   | 0.51      | 109                   |
| DiP     | 0.39        | 113                   | 0.29      | 113                   |
| MP      | 0.38        | 158                   | 0.39      | 170                   |
| TNBP    | 0.50        | 276                   | 0.53      | 260                   |
| RISP    | 0.59        | 213                   | 0.61      | 198                   |
| AP      | 0.59        | 119                   | 0.57      | 97                    |
| BeP     | 0.71        | 113                   | 0.72      | 121                   |
| RONP    | 0.58        | 249                   | 0.48      | 255                   |

For the CDP, BaP, SP, VBP, DaP, DiP, MP, and AP, all of which are formed adjacent to fast ice or a glacier tongue, the daily polynya area  $S_d$  is best correlated with the wind component that causes divergent ice motion away from a boundary comprising both coastline and fast ice (Fig. 8). This demonstrates the key role of fast ice in the formation and variability of the polynyas. For the CDP and MP, the direction of the wind component with the highest correlation corresponds well with the prevailing wind direction and the extent of fast ice or glacier tongues is relatively large. These factors may help explain why these polynyas become particularly large (Table 1) and major AABW formation areas. These results do not change significantly even if another atmospheric dataset is used (Table 3).

For the MBP, TNBP, RISP, and RONP, the daily polynya area  $S_d$  tends to be best correlated with the offshore wind component that causes divergent ice motion away from the coastline (Fig. 8). For the RISP and RONP, where the effects of synoptic wind on variability in polynya area are suggested to be strong (Markus and Burns 1995; Comiso et al. 2011; Drucker et al. 2011), the correlation coefficients  $r$  are relatively high (Table 3). For the RISP, the direction of the wind component with the highest correlation

corresponds well with the prevailing wind direction (Fig. 8), which makes this polynya the largest one (Table 1). In contrast, for the RONP, the direction of the wind component with the highest correlation does not correspond to the prevailing wind direction. This likely causes the large difference of their polynya area (Table 1; Drucker et al. 2011), in spite of their geographical similarity.

### c. Polynya ice production and its relationship with atmospheric conditions

Sea ice production, which leads to dense water and AABW formation, is estimated based on heat flux calculation using AMSR-E data by a similar method to the previous studies (Ohshima et al. 2003; Tamura et al. 2008; Nihashi et al. 2009, 2012; Iwamoto et al. 2014). Sea ice production rate  $V_i$  is estimated by assuming that heat from the ocean below is negligible and that all of the heat loss to the atmosphere goes toward freezing, given by

$$V_i = \frac{Q}{\rho_i L_f}, \quad (3)$$

where  $Q$  ( $\text{W m}^{-2}$ ) is heat loss to the atmosphere in the grid cell,  $\rho_i$  ( $=920 \text{ kg m}^{-3}$ ) is the density of sea ice, and  $L_f$  ( $=0.334 \text{ MJ kg}^{-1}$ ) is the latent heat of fusion for sea ice. The  $L_f$  value is based on Martin (1981) and has been used in many studies (e.g., Cavalieri and Martin 1994; Fusco et al. 2002). The value of  $Q$  is obtained by assuming that the sum of radiative and turbulent fluxes at the ice surface is balanced by the conductive heat flux in the ice whose thickness is derived from AMSR-E data using Eqs. (1) and (2). The procedure of the heat flux calculation is similar to that in estimation of thermal ice thickness from nighttime MODIS data, except for inclusion of shortwave radiation. Specifically, the clear-sky incoming shortwave radiation is calculated based on Zillman (1972), with modification for the cloud cover (Reed 1977). We used the total cloud cover defined from the ERA-Interim dataset.

A map of annual sea ice production (ice production cumulated from March to October) averaged over 2003–10 is shown in Fig. 9. Annual sea ice production in the major polynyas is summarized in Table 1. Errors in the ice production are considered to be mainly caused by atmospheric input and ice thickness errors. As it is difficult to estimate errors in the reanalysis data in the Antarctic Ocean, sensitivity tests for the atmospheric data were carried out using difference between the reanalysis datasets. The maximum point-by-point differences between ERA-Interim and NCEP CFSR

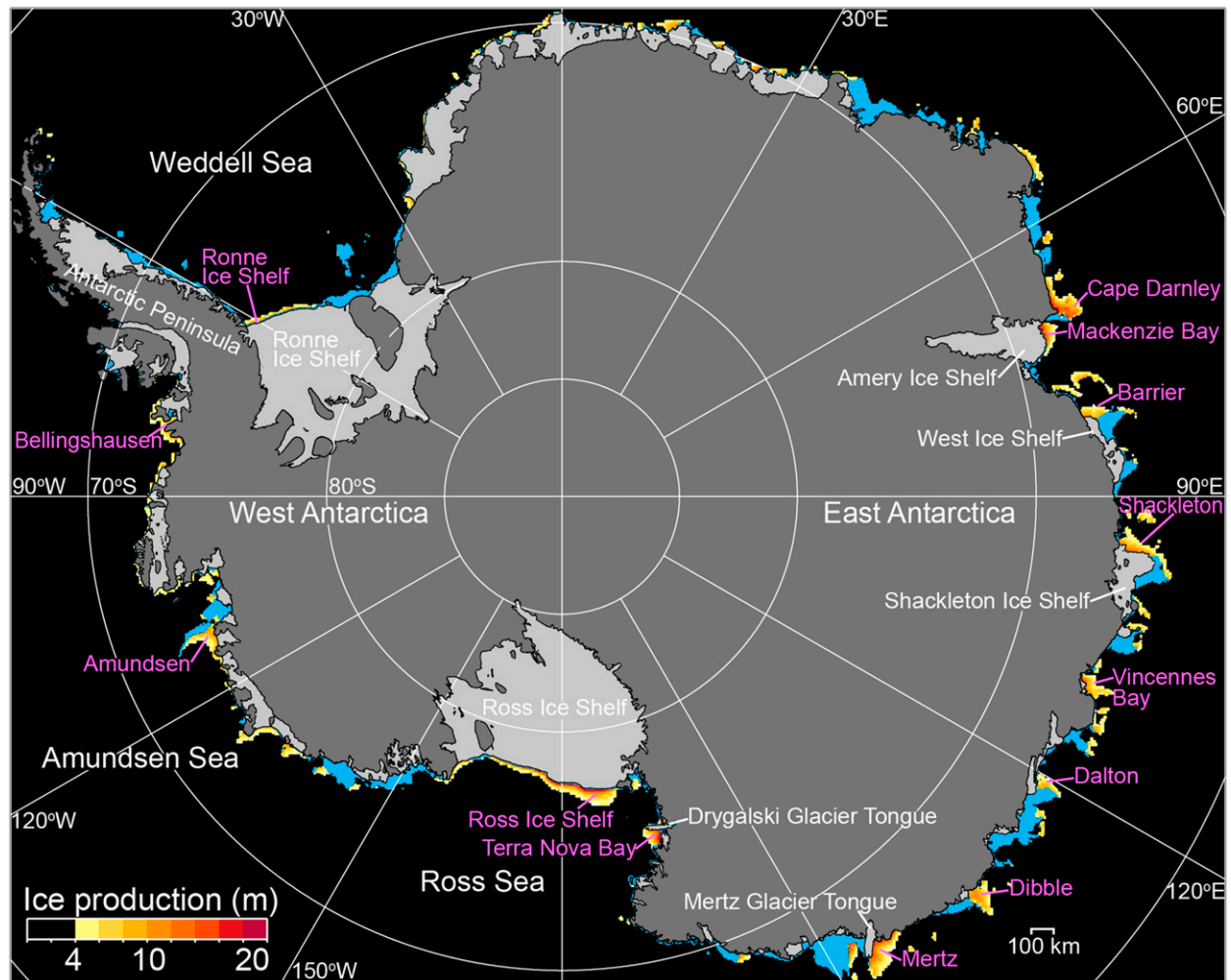


FIG. 9. Map of annual sea ice production (ice production cumulated from March to October) averaged over 2003–10. The fast ice areas shown in Fig. 5 are superimposed in sky blue.

datasets (NCEP CFSR minus ERA-Interim) averaged from March to October during 2003–10 in the Antarctic Ocean ( $>60^{\circ}\text{S}$ ) are as follows:  $-3.6\text{ K}$  at the grid point  $76.5^{\circ}\text{S}$ ,  $165^{\circ}\text{W}$  and  $+3.2\text{ K}$  at the grid point  $73.5^{\circ}\text{S}$ ,  $111^{\circ}\text{W}$  for air temperature at 2-m height;  $-1.6\text{ m s}^{-1}$  at the grid point  $73.5^{\circ}\text{S}$ ,  $130.5^{\circ}\text{W}$  and  $+1.5\text{ m s}^{-1}$  at the grid point  $67.5^{\circ}\text{S}$ ,  $71.5^{\circ}\text{E}$  for wind speed at 10-m height;  $-0.21$  at the grid point  $75.5^{\circ}\text{S}$ ,  $168^{\circ}\text{E}$  and  $+0.06$  at the grid point  $69^{\circ}\text{S}$ ,  $22^{\circ}\text{E}$  for the total cloud cover. These values are used for the sensitivity tests. Further, the

sensitivity to errors in ice thickness is examined by changing the thickness by  $\pm 0.06\text{ m}$ , based on root-mean-square deviation between ice thicknesses from Eqs. (1) and (2) and  $h_i$  from MODIS. Table 4 summarizes the sensitivity analyses. The largest ambiguity of the ice production arises from ice thickness (by about 30%–50%). The air temperature also causes considerable ambiguity because sensible heat loss to the atmosphere is a major component of the heat budget during winter. This sensitivity analysis indicates

TABLE 4. Sensitivities in annual ice production averaged over the 13 major coastal polynyas to the input data. Data during the freezing period (March–October) for the period 2003–10 are used.

|                              | Air temp                    | Wind speed                  | Total cloud   | Ice thickness          |
|------------------------------|-----------------------------|-----------------------------|---------------|------------------------|
| Perturbed value              | $-3.6/+3.2^{\circ}\text{C}$ | $-1.6/+1.5\text{ m s}^{-1}$ | $-0.21/+0.06$ | $-0.06/+0.06\text{ m}$ |
| Change in ice production (%) | $+20/-17$                   | $-8/+7$                     | $+3/-1$       | $+52/-29$              |

TABLE 5. Annual ice production (ice production cumulated from March to October) averaged over 2003–07 with its annual standard deviation for the major coastal polynyas. The ice production was estimated using the AMSR-E and SSM/I data (Tamura et al. 2011). Analysis areas are designated by yellow lines in Fig. 8; the areas are defined following the previous study (Tamura et al. 2008).

| Polynya | AMSR-E ( $10^{10} \text{ m}^3$ ) | SSM/I ( $10^{10} \text{ m}^3$ ) |
|---------|----------------------------------|---------------------------------|
| CDP     | $13.8 \pm 1.0$                   | $15.1 \pm 2.2$                  |
| MBP     | $6.0 \pm 0.7$                    | $7.4 \pm 1.1$                   |
| BaP     | $6.3 \pm 0.5$                    | $8.3 \pm 1.0$                   |
| SP      | $8.3 \pm 1.0$                    | $10.0 \pm 0.9$                  |
| VBP     | $6.5 \pm 0.5$                    | $7.9 \pm 0.8$                   |
| DaP     | $3.6 \pm 0.3$                    | $4.2 \pm 0.5$                   |
| DiP     | $5.3 \pm 0.6$                    | $5.7 \pm 0.6$                   |
| MP      | $13.2 \pm 1.5$                   | $13.4 \pm 2.3$                  |
| TNBP    | $5.7 \pm 0.6$                    | $5.5 \pm 1.1$                   |
| RISP    | $30.8 \pm 2.3$                   | $32.1 \pm 4.0$                  |
| AP      | $8.6 \pm 1.3$                    | $10.4 \pm 1.5$                  |
| BeP     | $5.3 \pm 1.4$                    | $2.6 \pm 0.8$                   |
| RONP    | $4.2 \pm 1.9$                    | $7.1 \pm 3.1$                   |

that better estimation of ice thickness is most important for accurate estimation of ice production.

The spatial distributions of the sea ice production in coastal polynya areas are generally consistent with the previous studies in which SSM/I data were used (Tamura et al. 2008, 2011). However, the AMSR-E ice production can reveal more detailed spatial distribution. Further, false sea ice production in the fast ice pixels caused by SSM/I is improved because AMSR-E can detect fast ice that cannot be resolved by SSM/I. A comparison of ice production in major coastal polynyas between AMSR-E and SSM/I is summarized in Table 5. For the comparison, we used the SSM/I ice production by Tamura et al. (2011) in which the same  $L_f$  value of  $0.334 \text{ MJ kg}^{-1}$  was used. The previous SSM/I ice production by Tamura et al. (2008) would be about 10% larger than that of this study, because the smaller  $L_f$  value of  $0.303 \text{ MJ kg}^{-1}$  was used. The AMSR-E ice production from this study tends to be slightly smaller than the SSM/I ice production. It should be noted that an atmospheric dataset with a coarse resolution of  $1.5^\circ \times 1.5^\circ$  was used for the SSM/I ice production. The difference in the atmospheric dataset also influences both the thin ice thickness estimation and the ice production estimation.

For each polynya, daily sea ice production  $V_d$  is compared with the daily polynya area  $S_d$  and near-surface atmospheric conditions from ERA-Interim to examine the determining factor for the variation of  $V_d$  (Table 6). It is shown that  $V_d$  is highly correlated with  $S_d$ , as expected. Correspondingly,  $V_d$  tends to be positively correlated with  $U_{\text{rmax}}$ . Turbulent heat loss to the atmosphere is mainly determined by air temperature at

TABLE 6. Summary of correlation coefficients between sea ice production  $V_d$  and the polynya area  $S_d$  and with near-surface atmospheric conditions for the major coastal polynyas. The terms  $U_{\text{rmax}}$ ,  $T$ , and  $U$  indicate the geostrophic wind components that best correlates with  $S_d$ , the air temperature at 2-m height, and the wind speed at 10-m height, respectively. Daily data during wintertime (May–August) from 2003 to 2011 are used. Analysis areas for  $V_d$  and  $S_d$  are designated by yellow lines in Fig. 8. The ERA-Interim data at the nearest grid point to each polynya (the starting point of green vector in Fig. 8) are used for  $U_{\text{rmax}}$ ,  $T$ , and  $U$ . Correlation coefficient values with a significance level of 99.5% are indicated by the boldface text, assuming that all the 1107 samples of daily data are regarded as independent data.

| Polynya | Correlation coefficient |                            |              |              |
|---------|-------------------------|----------------------------|--------------|--------------|
|         | $V_d$ vs $S_d$          | $V_d$ vs $U_{\text{rmax}}$ | $V_d$ vs $T$ | $V_d$ vs $U$ |
| CDP     | <b>0.83</b>             | <b>0.08</b>                | <b>-0.10</b> | <b>0.30</b>  |
| MBP     | <b>0.94</b>             | <b>0.61</b>                | <b>-0.48</b> | <b>0.37</b>  |
| BaP     | <b>0.85</b>             | <b>0.23</b>                | <b>-0.08</b> | <b>0.12</b>  |
| SP      | <b>0.84</b>             | <b>0.23</b>                | <b>-0.23</b> | 0.01         |
| VBP     | <b>0.72</b>             | <b>0.40</b>                | <b>-0.33</b> | <b>0.26</b>  |
| DaP     | <b>0.84</b>             | <b>0.39</b>                | -0.04        | <b>0.23</b>  |
| DiP     | <b>0.80</b>             | <b>0.24</b>                | <b>-0.34</b> | <b>0.19</b>  |
| MP      | <b>0.85</b>             | <b>0.35</b>                | <b>-0.21</b> | <b>0.19</b>  |
| TNBP    | <b>0.93</b>             | <b>0.58</b>                | <b>0.13</b>  | <b>0.47</b>  |
| RISP    | <b>0.91</b>             | <b>0.59</b>                | <b>0.19</b>  | <b>0.39</b>  |
| AP      | <b>0.69</b>             | <b>0.58</b>                | <b>-0.35</b> | <b>0.27</b>  |
| BeP     | <b>0.80</b>             | <b>0.69</b>                | <b>-0.41</b> | <b>0.39</b>  |
| RONP    | <b>0.93</b>             | <b>0.52</b>                | -0.04        | <b>0.38</b>  |

2-m height  $T$  and wind speed at 10-m height  $U$ ;  $V_d$  is negatively correlated with  $T$  and is positively correlated with  $U$ , except for the TNBP and RISP. From a multiple linear regression analysis in which  $V_d$  is treated as the dependent variable and  $U_{\text{rmax}}$ ,  $T$ , and  $U$  as the explanation variables (Table 7),  $U_{\text{rmax}}$  and  $T$  are shown to be the dominant factors that determine  $V_d$  in most polynyas. The coefficient of determination  $R^2$  tends to be small in many polynyas that formed adjacent to fast ice or glacier tongues such as the CDP, BaP, SP, DaP, DiP, and MP, suggesting that the three atmospheric parameters are not sufficient to explain the  $V_d$  variation. This is partly because katabatic wind is not reproduced in the ERA-Interim dataset. The katabatic wind has been suggested as a key factor for the coastal polynya formation, as studied in the MP area by Adolphs and Wendler (1995) and in the TNBP area by Bromwich and Kurtz (1984). However, effects of the katabatic wind do not necessarily seem dominant in some polynyas such as the CDP, BaP, and DaP (Massom et al. 1998). In such polynyas, the small  $R^2$  implies another mechanism of polynya formation. Especially in the CDP, only a small proportion (15%) of the  $V_d$  variation can be attributed to the three parameters despite its being the second largest sea ice production area (Table 1). Further, the daily change in

TABLE 7. Summary of a multiple linear regression analysis for the major coastal polynyas. In this analysis, the sea ice production  $V_d$  is the dependent variable and the geostrophic wind component that best correlates with the polynya area  $U_{\text{rmax}}$ , the air temperature at 2-m height  $T$ , and the wind speed at 10-m height  $U$  are the explanation variables. The terms  $\beta_{U_{\text{rmax}}}$ ,  $\beta_T$ , and  $\beta_U$  are the standardized partial regression coefficients of the  $U_{\text{rmax}}$ ,  $T$ , and  $U$ , respectively. The  $\beta$  values with a significance level of 99.5% are indicated by the boldface text. Also,  $R^2$  is the coefficient of determination. Daily data during wintertime (May–August) from 2003 to 2011 are used. Analysis areas for  $V_d$  are designated by yellow lines in Fig. 8. The ERA-Interim data at the nearest grid point to each polynya (the starting point of green vector in Fig. 8) are used for  $U_{\text{rmax}}$ ,  $T$ , and  $U$ .

| Polynya | $\beta_{U_{\text{rmax}}}$ | $\beta_T$ | $\beta_U$   | $R^2$ |
|---------|---------------------------|-----------|-------------|-------|
| CDP     | <b>0.15</b>               | −0.33     | <b>0.35</b> | 0.15  |
| MBP     | <b>0.44</b>               | −0.35     | <b>0.35</b> | 0.57  |
| BaP     | <b>0.73</b>               | −0.75     | <b>0.17</b> | 0.25  |
| SP      | <b>0.53</b>               | −0.61     | <b>0.13</b> | 0.26  |
| VBP     | <b>0.48</b>               | −0.56     | <b>0.19</b> | 0.43  |
| DaP     | <b>0.51</b>               | −0.40     | <b>0.17</b> | 0.25  |
| DiP     | <b>0.37</b>               | −0.54     | <b>0.19</b> | 0.30  |
| MP      | <b>0.31</b>               | −0.27     | <b>0.13</b> | 0.19  |
| TNBP    | <b>0.48</b>               | 0.00      | <b>0.17</b> | 0.36  |
| RISP    | <b>0.54</b>               | −0.02     | <b>0.13</b> | 0.37  |
| AP      | <b>0.52</b>               | −0.46     | <b>0.19</b> | 0.51  |
| BeP     | <b>0.54</b>               | −0.43     | <b>0.28</b> | 0.66  |
| RONP    | <b>0.47</b>               | −0.12     | <b>0.28</b> | 0.36  |

polynya area (see  $S_a$  and CV in Table 1) is relatively small for the CDP. We propose that the blocking effect of fast ice (and glacier tongues) on westward sea ice advection by the coastal current also can be a key factor for polynya formation.

#### d. Linkage between fast ice and coastal polynya

Time series of annual maps of Antarctic coastal polynyas and fast ice from 2003 to 2010 (not shown) can reveal their close linkage on interannual time scale: any drastic change in fast ice or glacier tongue causes a great impact on the adjacent polynya. Here we give some examples.

One is the substantial decrease in the MP area after the Mertz Glacier Tongue (MGT) calving (Fig. 10). The amount of sea ice production decreased by as much as 40% (Fig. 11), and the MP dropped from the third-largest to the fifth-largest Antarctic ice production polynya area, likely causing a reduction in AABW formation (Aoki et al. 2013). Our AMSR-E data with a higher spatial resolution detail this event more clearly than does SSM/I (Tamura et al. 2012). The MP had been formed on the western side of the MGT and offshore fast ice with grounded icebergs (Figs. 6g and 10b). This “ice cape” is usually formed from the tip of the MGT northward along the eastern edge of the Mertz Bank (Massom et al. 2001, 2010; Massom 2003). In February 2010, the iceberg B-9B, which had been

grounded in the area east of the MGT (Figs. 10a,b), crashed into the MGT, and the MGT calving occurred (Figs. 10c,d). After the calving, the coastal polynya that had been formed on the western side of the MGT disappeared (Figs. 10e,f). The AMSR-E data also reveal that the ice cape continued to determine polynya formation even after the calving, underlining the key role of fast ice on the polynya formation by blocking westward ice advection to cause divergence (Figs. 10e,f).

Another example is a coastal polynya formed near the BaP (Figs. 6b and 12), where dense water is expected to be formed (Galton-Fenzi et al. 2012). In this area, fast ice extent exhibits relatively large interannual variability along the Four Ladies Bank (FLB; Fig. 12), and interannual variability of sea ice production is mostly determined by the fast ice extent (Fig. 13). In the area east of the BaP, fast ice (FI-1) formed from the West Ice Shelf toward the north by the existence of grounded iceberg D-15, which acts as an “anchor point” (Fig. 12). In 2008, a relatively large grounded iceberg existed on the western side of the FLB, and fast ice was developed along the FLB from FI-1 to the iceberg (Figs. 11a and 12b). In 2009, lots of small grounded icebergs existed along the FLB, and fast ice was developed by the anchor points of these icebergs (Figs. 12c,d). On the other hand, the fast ice area is much smaller in 2010, and accordingly the polynya area is also smaller (Figs. 12e,f). For the eight years 2003–10, well-developed fast ice along the FLB is shown only in 2007 in addition to 2008 and 2009.

#### 4. Concluding remarks

This study presents the first combined circumpolar mapping and analysis of Antarctic coastal polynyas (sea ice production) and fast ice. This is based on the development of techniques to derive coincident coastal polynya and fast ice information from satellite AMSR-E passive microwave data, by exploiting the higher spatial resolution of these data compared to those of SSM/I used in earlier studies (Tamura et al. 2008; 2011). Previous studies were also limited to looking at fast ice and polynyas separately, or in a regionally limited fashion only.

In this study, the AMSR-E thin ice thickness algorithm has been developed based on comparisons between polarization ratio PR of AMSR-E TBs and thermal ice thickness  $h_i$  from MODIS in the RISP, RONP, and CDP, which are major source areas of AABW. According to the scatterplots of the PR versus  $h_i$  (Fig. 1), the thin ice thickness algorithm possibly contains an error of about 6 cm at maximum, indicating the regional differences (Table 2). It should be noted that, when such errors are taken into account, the

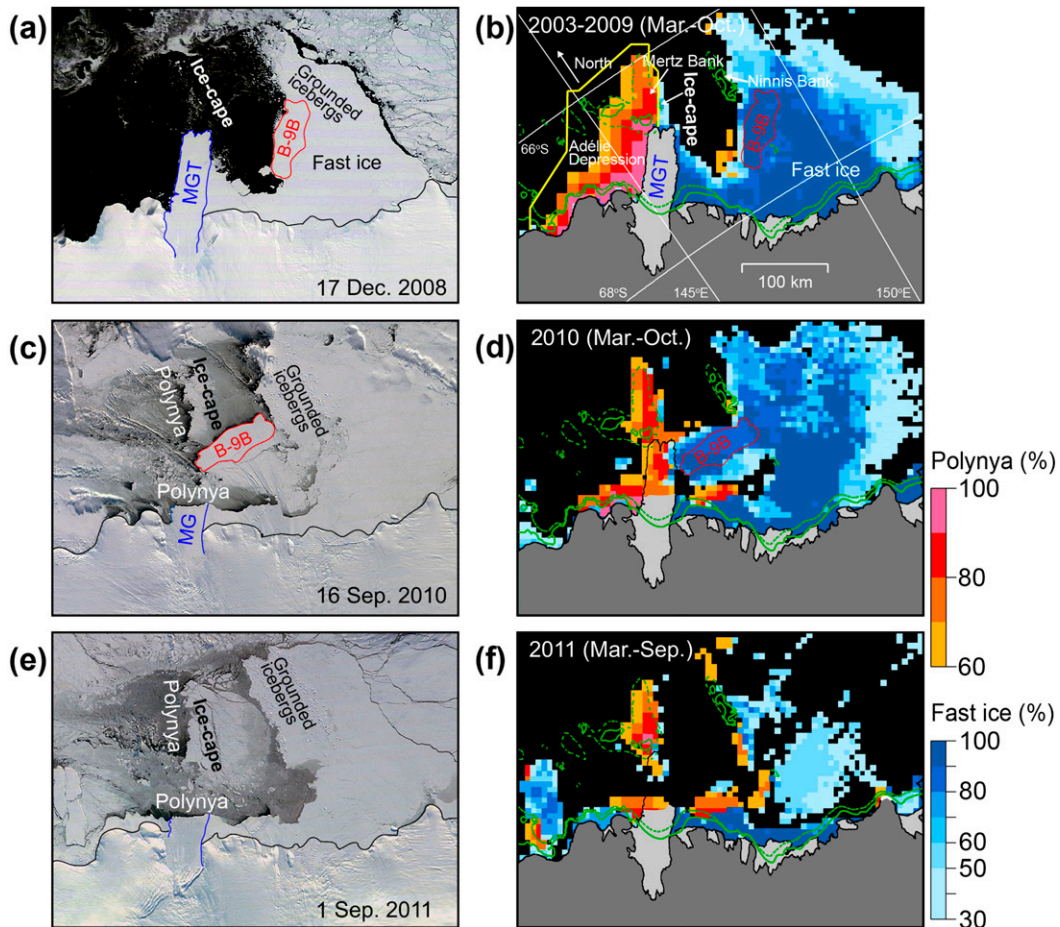


FIG. 10. Close-up maps of sea ice in the Mertz polynya area. (a),(c),(e) Visible images from MODIS obtained from the MODIS Rapid Response Project at NASA GSFC (<http://lance.nasa.gov/imagery/rapid-response/>). The coastline (black lines), the edge of the iceberg B-9B (red lines), and the Mertz Glacier Tongue (MGT)/Mertz Glacier (MG; blue lines) are traced on the MODIS images. Fast ice areas with small grounded icebergs are noted as “Grounded icebergs.” (b) Frequency of occurrence of coastal polynyas and fast ice from AMSR-E during the freezing period for the period 2003–09. The location of the iceberg B-9B is indicated by a red line based on the MODIS image in (a). (d) As in (b), but for data in 2010. (f) As in (b), but for data in 2011. In (b),(d), and (f), the 200- and 300-m bathymetric contours are indicated by solid and dotted green lines, respectively. The bathymetry was obtained from the General Bathymetric Chart of the Oceans (GEBCO) One Minute Grid.

estimation of sea ice production has the uncertainty of 30%–50% (Table 4). The relationship between PR and  $h_i$  in the Antarctic Ocean (Fig. 1) does not coincide exactly with that in the Arctic Ocean (Iwamoto et al. 2014). The biases of Antarctic minus Arctic cases are 1.8 cm at 89 GHz ( $\leq 10$  cm) and 5.2 cm at 36.5 GHz (10–20 cm) on average. Such differences, as well as the differences among the three polynyas, probably arise from a dominant sea ice type (e.g., frazil ice, grease ice, or nilas) in each area. The dominant sea ice type would be determined by local atmospheric conditions such as the surface air temperature and wind speed. Development of a more generalized algorithm such that the atmospheric conditions and geographical information are incorporated in addition to the PR values remains for

future work. For a more reliable algorithm, comparison and validation with ice thickness data by in situ observations will be ultimately required, although observations in the polynyas have been quite limited in the Antarctic Ocean until now. Such an enhanced algorithm would be applicable to all polar oceans.

A critical issue in the present study both for development of the algorithm and estimation of ice production is the reliability of the atmosphere dataset used. The ERA-Interim dataset used in our analysis is one of the most reliable atmospheric datasets (e.g., Jones and Lister 2015) covering the entire Antarctic Ocean and the whole AMSR-E period. However, the dataset cannot reproduce katabatic winds well. Atmospheric modeling study has shown that a model

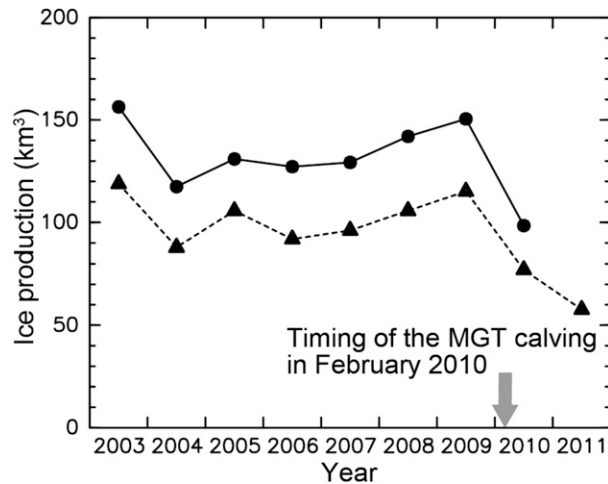


FIG. 11. Time series of sea ice production in the Adélie Depression area designated by yellow lines in Fig. 10b. Annual ice production (production cumulated from March to October) is shown from 2003 to 2010 (dots with a solid line). For comparison with 2011, when the data are available only until mid-September, ice production cumulated from March to August is also shown (triangles with a dashed line).

with a high spatial resolution can improve the representation of katabatic winds (Petrelli et al. 2008). In the future, incorporation of high-resolution atmospheric datasets that include the effect of katabatic wind will be required for more exact estimation of ice production as well as for further development of the thin ice thickness algorithm.

The circumpolar map of Fig. 5 is the centerpiece and most important figure of this study. It clearly reveals that most (10 of 13; the exceptions are MBP, RISP, and RONP) high ice production polynyas form on the western side of fast ice (and glacier tongues). A circumpolar analysis using the mapped time series and meteorological reanalysis data quantifies this relationship for all of the major Antarctic polynyas for the first time. The prevailing wind direction near the Antarctic coast (Fig. 8) is mostly westward and not northward (offshoreward), causing divergent ice motion away from the coastline. Nevertheless, coastal polynyas with high ice production (Table 1) are formed in several areas. The maps presented in this study (Figs. 5 and 6) clearly demonstrate that fast ice (and glacier tongues) protruding into the ocean is a key factor for the formation of many of the Antarctic coastal polynyas, since they cause divergent ice motion even if the westward (alongshore direction) wind is prevailing. On the other hand, in some of coastal polynyas formed on the western side of fast ice, only a small portion of daily change in the ice production can be explained by the surface atmospheric conditions (Table 7). This indicates that the blocking effect of fast ice (and glacier tongues) on westward sea

ice advection by the coastal current is likely another key factor for the formation of these polynyas. Such an effect seems particularly important for the protruding fast ice formed by grounded icebergs acting as the anchor points (Fraser et al. 2012), as in the cases of the CDP, MP, and BaP (Figs. 4e, 4f, 10, and 12). Because the source of these icebergs is the vast Antarctic ice shelves, such protruding fast ice is a remarkable feature of the Antarctic Ocean, and different from the Arctic case.

This study has also demonstrated that a drastic change in fast ice extent, which is particularly vulnerable to oceanic and atmospheric conditions, can cause dramatic changes in sea ice production (Figs. 10–13) and possibly AABW formation that can potentially contribute to further climate change, as in the case of the MGT calving (e.g., Kushahara et al. 2011; Tamura et al. 2012; Lacarra et al. 2014). The mapping presented in this study (Fig. 5) reveals that many of the coastal polynyas are formed along the East Antarctic coast where fast ice dominates. In the West Antarctic sector, it was suggested that intrusion of relatively warm Circumpolar Deep Water onto the continental shelf causes basal melting of ice shelves (Pritchard et al. 2012; Hellmer et al. 2012), possibly leading to acceleration of iceberg calving. Future climate change might lead a similar situation also in the East Antarctic sector (Miles et al. 2013), where the location of Circumpolar Deep Water is relatively close to the continent (Orsi et al. 1995). This possibly causes drastic changes of fast ice extent directly by melting or indirectly by acceleration of iceberg calving.

Although the AMSR-E mission ended in October 2011, continuous observation by AMSR-2 on JAXA's *Shizuku* satellite [*Global Change Observation Mission—Water 1 (GCOM-W1)*] launched in May 2012 is vitally effective for the monitoring to understand the processes of coastal polynyas and fast ice. When compared to SSM/I, which has been accumulated for more than 20 years, the disadvantage of AMSR-E and AMSR-2 to date is its shorter record period. Careful comparison of AMSR-2, AMSR-E, and SSM/I data and their combined study would partly overcome the disadvantage for investigation of the polynyas and their sea ice production, which will enable us to conduct climate-change-related analyses in the Antarctic Ocean.

Based on the results of this study, we propose that fast ice as well as coastal polynyas should be treated in future climate models, such as the models for the Intergovernmental Panel on Climate Change (IPCC) reports, to reproduce the formation and variability of sea ice production, dense water, and AABW properly. The mapping and dataset (monthly fast ice extent and daily sea ice production) presented in this study provide the boundary and validation

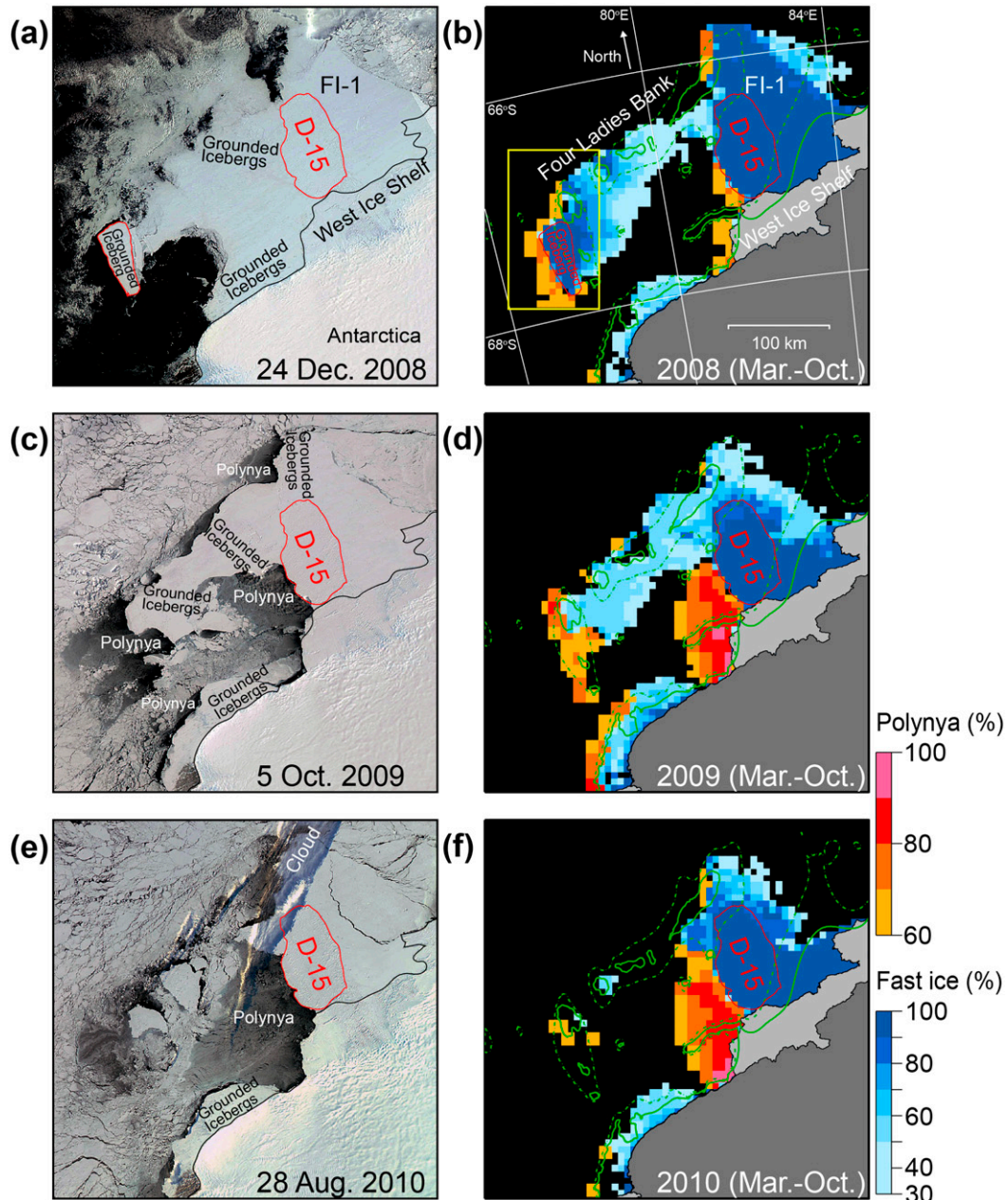


FIG. 12. Close-up maps of sea ice in the Barrier polynya area. (a),(c),(e) Visible images from MODIS. The coastline (black lines) and the edge of large grounded icebergs (red lines) are traced on the MODIS images. Fast ice areas with small grounded icebergs are noted as “Grounded icebergs.” (b),(d),(f) Frequency of occurrence of coastal polynyas and fast ice from AMSR-E during the freezing period in 2008–10. The locations of the large grounded icebergs are indicated by red line based on the MODIS images in (a),(c), and (e). The 200- and 300-m bathymetric contours are indicated by solid and dotted green lines, respectively.

data of fast ice and sea ice production for such models. The dataset created in this study is archived at the website of the Institute of Low Temperature Science, Hokkaido University (<http://wwwod.lowtem.hokudai.ac.jp/polar-seaflux>).

*Acknowledgments.* The AMSR-E data were provided by the National Snow and Ice Data Center (NSIDC),

University of Colorado. We thank Robert A. Massom and Alexander D. Fraser for their valuable comments, and Takeshi Tamura for helping with the development of the AMSR-E algorithms. Comments from the editor and three reviewers were very helpful. This work was supported by Grants-in-Aids for Scientific Research (20221001, 21740337, 24740322, and 25241001) of the

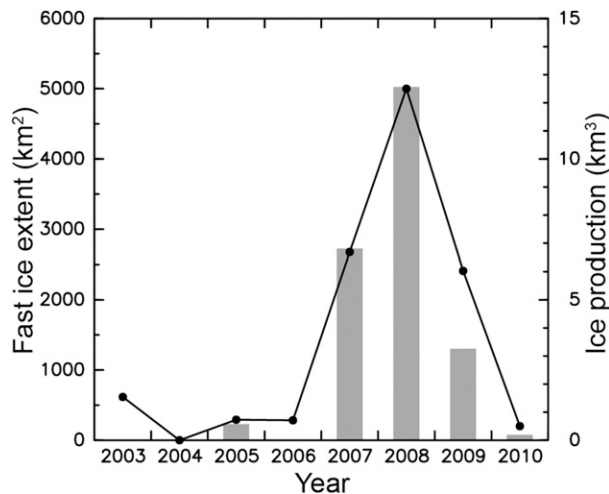


FIG. 13. Time series of fast ice extent (bars) and annual sea ice production (dots with the line) in a box designated by yellow lines in Fig. 12b. The fast ice extent is defined as the area where the frequency of occurrence of fast ice is  $\geq 25\%$ . The ice production is summed for the grid points with an annual ice production per unit area of  $\geq 7$  m.

Ministry of Education, Culture, Sports, Science and Technology in Japan. This work was also supported by a research fund for Global Change Observation Mission–Water 1 (GCOM-W1) of the Japan Aerospace Exploration Agency (JAXA).

#### REFERENCES

- Adolphs, U., and G. Wendler, 1995: A pilot study on the interactions between katabatic winds and polynyas at the Adélie Coast, eastern Antarctica. *Antarct. Sci.*, **7**, 307–314, doi:10.1017/S0954102095000423.
- Aoki, S., Y. Kitade, K. Shimada, K. I. Ohshima, T. Tamura, C. C. Bajish, M. Moteki, and S. R. Rintoul, 2013: Widespread freshening in the Seasonal Ice Zone near 140°E off the Adélie Land Coast, Antarctica, from 1994 to 2012. *J. Geophys. Res. Oceans*, **118**, 6046–6063, doi:10.1002/2013JC009009.
- Arrigo, K. R., and G. L. van Dijken, 2003: Phytoplankton dynamics within 37 Antarctic coastal polynya systems. *J. Geophys. Res.*, **108**, 3271, doi:10.1029/2002JC001739.
- Ashcroft, P., and F. Wentz, 2003: AMSR-E/Aqua L2A global swath spatially-resampled brightness temperatures (Tb) V002. National Snow and Ice Data Center, Boulder, CO. [Available online at [http://nsidc.org/data/ae\\_j2a.html](http://nsidc.org/data/ae_j2a.html).]
- Bromwich, D. H., and D. D. Kurtz, 1984: Katabatic wind forcing of the Terra Nova Bay polynya. *J. Geophys. Res.*, **89**, 3561–3572, doi:10.1029/JC089iC03p03561.
- Cavaleri, D. J., and S. Martin, 1994: The contribution of Alaskan, Siberian, and Canadian coastal polynyas to the cold halocline layer of the Arctic Ocean. *J. Geophys. Res.*, **99**, 18 343–18 362, doi:10.1029/94JC01169.
- , T. Markus, and J. C. Comiso, 2004: AMSR-E/Aqua daily L3 6.25 km 89 GHz brightness temperature polar grids V002. National Snow and Ice Data Center, Boulder, CO, accessed 1 August 2013. [Available online at [http://nsidc.org/data/ae\\_si6.html](http://nsidc.org/data/ae_si6.html).]
- Comiso, J. C., and A. L. Gordon, 1998: Interannual variability in summer sea ice minimum, coastal polynyas and bottom water formation in the Weddell Sea. *Antarctic Sea Ice: Physical Processes, Interactions, and Variability*, M. O. Jeffries, Ed., American Geophysical Union, Antarctic Research Series, Vol. 74, 293–315.
- , R. Kwok, S. Martin, and A. L. Gordon, 2011: Variability and trends in sea ice extent and ice production in the Ross Sea. *J. Geophys. Res.*, **116**, C04021, doi:10.1029/2010JC006391.
- Cox, G. F. N., and W. F. Weeks, 1983: Equations for determining the gas and brine volumes in sea ice samples. *J. Glaciol.*, **29**, 306–316.
- Dragon, A. C., M. N. Houssais, C. Herbaut, and J. B. Charrassin, 2014: A note on the intraseasonal variability in an Antarctic polynya: Prior to and after the Mertz Glacier calving. *J. Mar. Syst.*, **130**, 46–55, doi:10.1016/j.jmarsys.2013.06.006.
- Drucker, R., S. Martin, and R. Moritz, 2003: Observations of ice thickness and frazil ice in the St. Lawrence Island polynya from satellite imagery, upward looking sonar, and salinity/temperature moorings. *J. Geophys. Res.*, **108**, 3149, doi:10.1029/2001JC001213.
- , —, and R. Kwok, 2011: Sea ice production and export from coastal polynyas in the Weddell and Ross Seas. *Geophys. Res. Lett.*, **38**, L17502, doi:10.1029/2011GL048668.
- Fedotov, V. I., N. V. Cherepanov, and K. P. Tyshko, 1998: Some features of the growth, structure and metamorphism of East Antarctic landfast sea ice. *Antarctic Sea Ice: Physical Processes, Interactions, and Variability*, M. O. Jeffries, Ed., American Geophysical Union, Antarctic Research Series, Vol. 74, 343–354.
- Foster, T. D., and E. C. Carmack, 1976: Frontal zone mixing and Antarctic Bottom Water formation in the southern Weddell Sea. *Deep-Sea Res. Oceanogr. Abstr.*, **23**, 301–317, doi:10.1016/0011-7471(76)90872-X.
- Fraser, A. D., R. A. Massom, K. J. Michael, B. K. Galton-Fenzi, and J. L. Lieser, 2012: East Antarctic landfast sea ice distribution and variability, 2000–08. *J. Climate*, **25**, 1137–1156, doi:10.1175/JCLI-D-10-05032.1.
- Fusco, G., D. Flocco, G. Budillon, G. Spezie, and E. Zambianchi, 2002: Dynamics and variability of Terra Nova Bay Polynya. *PSZN Marine Ecology*, **23**, 201–209, doi:10.1111/j.1439-0485.2002.tb00019.x.
- Galton-Fenzi, B. K., J. R. Hunter, R. Coleman, S. J. Marsland, and R. C. Warner, 2012: Modeling the basal melting and marine ice accretion of the Amery Ice Shelf. *J. Geophys. Res.*, **117**, C09031, doi:10.1029/2012JC008214.
- Giles, A. B., R. A. Massom, and V. I. Lytle, 2008: Fast-ice distribution in East Antarctica during 1997 and 1999 determined using RADARSAT data. *J. Geophys. Res.*, **113**, C02S14, doi:10.1029/2007JC004139.
- Gordon, A. L., B. A. Huber, H. H. Hellmer, and A. Field, 1993: Deep and bottom water of the Weddell Sea's western rim. *Science*, **262**, 95–97, doi:10.1126/science.262.5130.95.
- Hall, D. K., J. R. Key, K. A. Casey, G. A. Riggs, and D. J. Cavalieri, 2004: Sea ice surface temperature product from MODIS. *IEEE Trans. Geosci. Remote Sens.*, **42**, 1076–1087, doi:10.1109/TGRS.2004.825587.
- Haran, T., J. Bohlander, T. Scambos, T. Painter, and M. Fahnestock, 2005: MODIS Mosaic of Antarctica (MOA) image map. National Snow and Ice Data Center, Boulder, CO, accessed 7 December 2011. [Available online at <http://nsidc.org/data/nsidc-0280.html>.]
- Hellmer, H. H., F. Kauker, R. Timmermann, J. Determann, and J. Rae, 2012: Twenty-first-century warming of a large Antarctic ice-shelf cavity by a redirected coastal current. *Nature*, **485**, 225–228, doi:10.1038/nature11064.

- Hoppema, M., and L. G. Anderson, 2007: Biogeochemistry of polynyas and their role in sequestration of anthropogenic constituents. *Polynyas: Windows to the World's Oceans*, W. O. Smith, Jr. and D. G. Barber, Eds., Elsevier, 193–221.
- Hwang, B. J., J. K. Ehn, D. G. Barber, R. Galley, and T. C. Grenfel, 2007: Investigations of newly formed sea ice in the Cape Bathurst polynya: 2. Microwave emission. *J. Geophys. Res.*, **112**, C05003, doi:10.1029/2006JC003703.
- Iwamoto, K., K. I. Ohshima, T. Tamura, and S. Nihashi, 2013: Estimation of thin ice thickness from AMSR-E data in the Chukchi Sea. *Int. J. Remote Sens.*, **34**, 468–489, doi:10.1080/01431161.2012.712229.
- , —, and —, 2014: Improved mapping of sea ice production in the Arctic Ocean using AMSR-E thin ice thickness algorithm. *J. Geophys. Res.*, **119**, 3574–3594, doi:10.1002/2013JC009749.
- Jacobs, S. S., A. F. Amos, and P. M. Bruchhausen, 1970: Ross Sea oceanography and Antarctic Bottom Water formation. *Deep-Sea Res. Oceanogr. Abstr.*, **17**, 935–962, doi:10.1016/0011-7471(70)90046-X.
- Jeffries, M. O., and U. Adolphs, 1997: Early winter ice and snow thickness distribution, ice structure and development of the western Ross Sea pack ice between the ice edge and the Ross Ice Shelf. *Antarct. Sci.*, **9**, 188–200, doi:10.1017/S0954102097000242.
- Jones, P. D., and D. H. Lister, 2015: Antarctic near-surface air temperatures compared with ERA-Interim values since 1979. *Int. J. Climatol.*, doi:10.1002/joc.4061, in press.
- Kern, S., 2009: Wintertime Antarctic coastal polynya area: 1992–2008. *Geophys. Res. Lett.*, **36**, L14501, doi:10.1029/2009GL038062.
- , G. Spreen, L. Kaleschke, and G. Heygster, 2007: Polynya Signature Simulation Method polynya area in comparison to AMSR-E 89 GHz sea-ice concentrations in the Ross Sea and off the Adelie Coast, Antarctica, for 2002–05: First results. *Ann. Glaciol.*, **46**, 409–418, doi:10.3189/172756407782871585.
- Key, J., J. B. Collins, C. Fowler, and R. S. Stone, 1997: High-latitude surface temperature estimates from thermal satellite data. *Remote Sens. Environ.*, **61**, 302–309, doi:10.1016/S0034-4257(97)89497-7.
- Killworth, P. D., 1983: Deep convection in the World Ocean. *Rev. Geophys.*, **21**, 1–26, doi:10.1029/RG021i001p00001.
- Kitade, Y., and Coauthors, 2014: Antarctic Bottom Water production from the Vincennes Bay Polynya, East Antarctica. *Geophys. Res. Lett.*, **41**, 3528–3534, doi:10.1002/2014GL059971.
- Kondo, J., 1975: Air–sea bulk transfer coefficient in diabatic conditions. *Bound-Layer Meteor.*, **9**, 91–112, doi:10.1007/BF00232256.
- König-Langlo, G., and E. Augstein, 1994: Parameterization of the downward longwave radiation at the Earth's surface in polar regions. *Meteor. Z.*, **3**, 343–347.
- Kottmeier, C., and L. Sellmann, 1996: Atmospheric and oceanic forcing of Weddell Sea ice motion. *J. Geophys. Res.*, **101**, 20 809–20 824, doi:10.1029/96JC01293.
- Kovacs, A., 1996: Sea ice—Part I: Bulk salinity versus ice floe thickness. CRREL Monogr. 96-7, U.S. Army Corps of Engineers Cold Regions Research and Engineering Laboratory, Hanover, NH, 16 pp.
- Kozlovsky, A. M., Y. L. Nazintsev, V. I. Fedotov, and N. V. Cherepanov, 1977: Fast ice of the Eastern Antarctic (in Russian). *Proc. Soviet Antarct. Exped.*, **63**, 1–129.
- Kurtz, D. D., and D. H. Bromwich, 1985: A recurring, atmospherically forced polynya in Terra Nova Bay. *Oceanology of the Antarctic Continental Shelf*, S. S. Jacobs, Ed., American Geophysical Union, Antarctic Research Series, Vol. 43, 177–201.
- Kusahara, K., H. Hasumi, and G. D. Williams, 2011: Impact of Mertz Glacier Tongue calving on dense water formation and export. *Nat. Commun.*, **2**, 159, doi:10.1038/ncomms1156.
- Lacarra, M., M. N. Houssais, C. Herbaut, E. Sultan, and M. Beauverger, 2014: Dense shelf water production in the Adélie Depression, East Antarctica, 2004–2012: Impact of the Mertz Glacier calving. *J. Geophys. Res.*, **119**, 5203–5220, doi:10.1002/2013JC009124.
- Markus, T., and B. A. Burns, 1995: A method to estimate subpixel-scale coastal polynyas with satellite passive microwave data. *J. Geophys. Res.*, **100**, 4473–4487, doi:10.1029/94JC02278.
- , and D. J. Cavalieri, 2000: An enhancement of the NASA Team sea ice algorithm. *IEEE Trans. Geosci. Remote Sens.*, **38**, 1387–1398, doi:10.1109/36.843033.
- , C. Kottmeier, and E. Fahrbach, 1998: Ice formation in coastal polynyas in the Weddell Sea and their impact on oceanic salinity. *Antarctic Sea Ice: Physical Processes, Interactions, and Variability*, M. O. Jeffries, Ed., American Geophysical Union, Antarctic Research Series, Vol. 74, 273–292.
- Martin, S., 1981: Frazil ice in rivers and oceans. *Annu. Rev. Fluid Mech.*, **13**, 379–397, doi:10.1146/annurev.fl.13.010181.002115.
- , R. Drucker, R. Kwok, and B. Holt, 2004: Estimation of the thin ice thickness and heat flux for the Chukchi Sea Alaskan coast polynya from Special Sensor Microwave/Imager data, 1990–2001. *J. Geophys. Res.*, **109**, C10012, doi:10.1029/2004JC002428.
- Massom, R. A., 2003: Recent iceberg calving events in the Ninnis Glacier region, East Antarctica. *Antarct. Sci.*, **15**, 303–313, doi:10.1017/S0954102003001299.
- , P. T. Harris, K. J. Michael, and M. J. Potter, 1998: The distribution and formative processes of latent-heat polynyas in East Antarctica. *Ann. Glaciol.*, **27**, 420–426.
- , K. L. Hill, V. I. Lytle, A. P. Worby, M. J. Paget, and I. Allison, 2001: Effects of regional fast-ice and iceberg distributions on the behaviour of the Mertz Glacier polynya, East Antarctica. *Ann. Glaciol.*, **33**, 391–398, doi:10.3189/172756401781818518.
- , A. B. Giles, H. A. Fricker, R. C. Warner, B. Legrésy, G. Hyland, N. Young, and A. D. Fraser, 2010: Examining the interaction between multi-year landfast sea ice and the Mertz Glacier Tongue, East Antarctica: Another factor in ice sheet stability? *J. Geophys. Res.*, **115**, C12027, doi:10.1029/2009JC006083.
- Maykut, G. A., 1978: Energy exchange over young sea ice in the central Arctic. *J. Geophys. Res.*, **83**, 3646–3658, doi:10.1029/JC083iC07p03646.
- , and D. K. Perovich, 1987: The role of shortwave radiation in the summer decay of a sea ice cover. *J. Geophys. Res.*, **92**, 7032–7044, doi:10.1029/JC092iC07p07032.
- Miles, B. W. J., C. R. Stokes, A. Vieli, and N. J. Cox, 2013: Rapid, climate-driven changes in outlet glaciers on the Pacific coast of East Antarctica. *Nature*, **500**, 563–566, doi:10.1038/nature12382.
- Miller, L. A., and G. R. DiTullio, 2007: Gas fluxes and dynamics in polynyas. *Polynyas: Windows to the World's Oceans*, W. O. Smith, Jr. and D. G. Barber, Eds., Elsevier, 163–191.
- Morales Maqueda, M. A., A. J. Willmott, and N. R. T. Biggs, 2004: Polynya dynamics: A review of observations and modeling. *Rev. Geophys.*, **42**, RG1004, doi:10.1029/2002RG000116.
- Nakayama, Y., R. Timmermann, M. Schröder, and H. H. Hellmer, 2014: On the difficulty of modeling Circumpolar Deep Water intrusions onto the Amundsen Sea continental shelf. *Ocean Modell.*, **84**, 26–34, doi:10.1016/j.ocemod.2014.09.007.

- Nihashi, S., and K. I. Ohshima, 2001: Relationship between ice decay and solar heating through open water in the Antarctic sea ice zone. *J. Geophys. Res.*, **106**, 16 767–16 782, doi:10.1029/2000JC000399.
- , —, T. Tamura, Y. Fukamachi, and S. Saitoh, 2009: Thickness and production of sea ice in the Okhotsk Sea coastal polynyas from AMSR-E. *J. Geophys. Res.*, **114**, C10025, doi:10.1029/2008JC005222.
- , —, and N. Kimura, 2012: Creation of a heat and salt flux dataset associated with sea ice production and melting in the Sea of Okhotsk. *J. Climate*, **25**, 2261–2278, doi:10.1175/JCLI-D-11-00022.1.
- Ohshima, K. I., T. Watanabe, and S. Nihashi, 2003: Surface heat budget of the Sea of Okhotsk during 1987–2001 and the role of sea ice on it. *J. Meteor. Soc. Japan*, **81**, 653–677, doi:10.2151/jmsj.81.653.
- , and Coauthors, 2013: Antarctic Bottom Water production by intense sea-ice formation in the Cape Darnley polynya. *Nat. Geosci.*, **6**, 235–240, doi:10.1038/ngeo1738.
- Orsi, A. H., T. Whitworth III, and W. D. Nowlin Jr., 1995: On the meridional extent and fronts of the Antarctic Circumpolar Current. *Deep-Sea Res. I*, **42**, 641–673, doi:10.1016/0967-0637(95)00021-W.
- Pease, C. H., 1987: The size of wind-driven coastal polynyas. *J. Geophys. Res.*, **92**, 7049–7059, doi:10.1029/JC092iC07p07049.
- Petrelli, P., N. L. Bindoff, and A. Bergamasco, 2008: The sea ice dynamics of Terra Nova Bay and Ross Ice Shelf Polynyas during a spring and winter simulation. *J. Geophys. Res.*, **113**, C09003, doi:10.1029/2006JC004048.
- Pritchard, H. D., S. R. M. Ligtenberg, H. A. Fricker, D. G. Vaughan, M. R. van den Broeke, and L. Padman, 2012: Antarctic ice-sheet loss driven by basal melting of ice shelves. *Nature*, **484**, 502–505, doi:10.1038/nature10968.
- Reed, R. K., 1977: On estimating insolation over the ocean. *J. Phys. Oceanogr.*, **7**, 482–485, doi:10.1175/1520-0485(1977)007<0482:OEIOTO>2.0.CO;2.
- Renfrew, I. A., J. C. King, and T. Markus, 2002: Coastal polynyas in the southern Weddell Sea: Variability of the surface energy budget. *J. Geophys. Res.*, **107**, 3063, doi:10.1029/2000JC000720.
- Riggs, G. A., D. K. Hall, and V. V. Salomonson, 2006: MODIS sea ice products user guide to collection 5. NASA Goddard Space Flight Center, Greenbelt, MD, 49 pp. [Available online at [http://modis-snow-ice.gsfc.nasa.gov/uploads/siug\\_c5.pdf](http://modis-snow-ice.gsfc.nasa.gov/uploads/siug_c5.pdf).]
- Rintoul, S. R., 1998: On the origin and influence of Adélie Land Bottom Water. *Ocean, Ice, and Atmosphere: Interactions at the Antarctic Continental Margin*, S. S. Jacobs and R. F. Weiss, Eds., American Geophysical Union, Antarctic Research Series, Vol. 75, 151–171.
- Saha, S., and Coauthors, 2010: NCEP Climate Forecast System Reanalysis (CFSR) 6-hourly products, January 1979 to December 2010. Research Data Archive at the National Center for Atmospheric Research, Computational and Information Systems Laboratory, accessed 31 Oct 2014, doi:10.5065/D69K487J.
- Scambos, T. A., T. M. Haran, and R. Massom, 2006: Validation of AVHRR and MODIS ice surface temperature products using in situ radiometer. *Ann. Glaciol.*, **44**, 345–351, doi:10.3189/172756406781811457.
- Scott, K. A., M. Buehner, and T. Carrieres, 2014: An assessment of sea-ice thickness along the Labrador coast from AMSR-E and MODIS data for operational data assimilation. *IEEE Trans. Geosci. Remote Sens.*, **52**, 2726–2737, doi:10.1109/TGRS.2013.2265091.
- Shadwick, E. H., and Coauthors, 2013: Glacier tongue calving reduced dense water formation and enhanced carbon uptake. *Geophys. Res. Lett.*, **40**, 904–909, doi:10.1002/grl.50178.
- Tamura, T., and K. I. Ohshima, 2011: Mapping of sea ice production in the Arctic coastal polynyas. *J. Geophys. Res.*, **116**, C07030, doi:10.1029/2010JC006586.
- , —, H. Enomoto, K. Tateyama, A. Muto, S. Ushio, and R. A. Massom, 2006: Estimation of thin sea-ice thickness from NOAA AVHRR data in a polynya off the Wilkes Land coast, East Antarctica. *Ann. Glaciol.*, **44**, 269–274, doi:10.3189/172756406781811745.
- , —, T. Markus, D. J. Cavalieri, S. Nihashi, and N. Hirasawa, 2007: Estimation of thin ice thickness and detection of fast ice from SSM/I data in the Antarctic Ocean. *J. Atmos. Oceanic Technol.*, **24**, 1757–1772, doi:10.1175/JTECH2113.1.
- , —, and S. Nihashi, 2008: Mapping of sea ice production for Antarctic coastal polynyas. *Geophys. Res. Lett.*, **35**, L07606, doi:10.1029/2007GL032903.
- , —, —, and H. Hasumi, 2011: Estimation of surface heat/salt fluxes associated with sea ice growth/melt in the Southern Ocean. *SOLA*, **7**, 17–20, doi:10.2151/sola.2011-005.
- , G. D. Williams, A. D. Fraser, and K. I. Ohshima, 2012: Potential regime shift in decreased sea ice production after the Mertz Glacier calving. *Nat. Commun.*, **3**, 826, doi:10.1038/ncomms1820.
- Thorndike, A. S., and R. Colony, 1982: Sea ice motion in response to geostrophic winds. *J. Geophys. Res.*, **87**, 5845–5852, doi:10.1029/JC087iC08p05845.
- Toyota, T., S. Takatsuji, K. Tateyama, K. Naoki, and K. I. Ohshima, 2007: Properties of sea ice and overlying snow in the southern Sea of Okhotsk. *J. Oceanogr.*, **63**, 393–411, doi:10.1007/s10872-007-0037-2.
- Uotila, J., T. Vihma, and J. Launiainen, 2000: Response of the Weddell Sea pack ice to wind forcing. *J. Geophys. Res.*, **105**, 1135–1151, doi:10.1029/1999JC900265.
- Vihma, T., J. Launiainen, and J. Uotila, 1996: Weddell Sea ice drift: Kinematics and wind forcing. *J. Geophys. Res.*, **101**, 18 279–18 296, doi:10.1029/96JC01441.
- Williams, G. D., N. L. Bindoff, S. J. Marsland, and S. R. Rintoul, 2008: Formation and export of dense shelf water from the Adélie Depression, East Antarctica. *J. Geophys. Res.*, **113**, C04039, doi:10.1029/2007JC004346.
- , S. Aoki, S. S. Jacobs, S. R. Rintoul, T. Tamura, and N. L. Bindoff, 2010: Antarctic Bottom Water from the Adélie and George V Land coast, East Antarctica (140°–149°E). *J. Geophys. Res.*, **115**, C04027, doi:10.1029/2009JC005812.
- WMO, 1970: WMO sea-ice nomenclature, terminology, codes and illustrated glossary. WMO/OMM/BMO Rep. 259, Tech. Paper 145, World Meteorological Organization, 147 pp.
- Yu, Y., and D. A. Rothrock, 1996: Thin ice thickness from satellite thermal imagery. *J. Geophys. Res.*, **101**, 25 753–25 766, doi:10.1029/96JC02242.
- Zillman, J. W., 1972: A study of some aspects of the radiation and heat budgets of the Southern Hemisphere oceans. Department of the Interior, Bureau of Meteorology, Canberra, Meteorological Studies Series, Vol. 26, 562 pp.
- Zwally, H. J., J. C. Comiso, and A. L. Gordon, 1985: Antarctic offshore leads and polynyas and oceanographic effects. *Oceanology of the Antarctic Continental Shelf*, S. S. Jacobs, Ed., American Geophysical Union, Antarctic Research Series, Vol. 43, 203–226.